Ferromagnetism and Conductivity in Atomically Thin $SrRuO_3$

H. Boschker,[1] T. Harada,[1] T. Asaba,[2] R. Ashoori,[3] A. V. Boris,[1] H. Hilgenkamp,[4] C. R. Hughes,[1,5] M. E. Holtz,[6] L. Li,[2,3] D. A. Muller,[6,7] H. Nair,[8] P. Reith,[4] X. Renshaw Wang,[4,*] D. G. Schlom,[7,8] A. Soukiassian,[8] and J. Mannhart[1]

[1]*Max Planck Institute for Solid State Research, 70569 Stuttgart, Germany*
[2]*Department of Physics, University of Michigan, Ann Arbor, Michigan 48109, USA*
[3]*Department of Physics, Massachusetts Institute of Technology, Cambridge, Massachusetts 02139, USA*
[4]*MESA+ Institute for Nanotechnology, University of Twente, Enschede, Netherlands*
[5]*Experimental Physics VI, Center for Electronic Correlations and Magnetism, Augsburg University, 86135 Augsburg, Germany*
[6]*School of Applied and Engineering Physics, Cornell University, Ithaca, New York 14853, USA*
[7]*Kavli Institute at Cornell for Nanoscale Science, Ithaca, New York 14853, USA*
[8]*Department of Materials Science and Engineering, Cornell University, Ithaca, New York 14853, USA*

(Received 25 July 2018; revised manuscript received 22 October 2018; published 8 February 2019)

Atomically thin ferromagnetic and conducting electron systems are highly desired for spintronics, because they can be controlled with both magnetic and electric fields. We present $(SrRuO_3)_1 - (SrTiO_3)_5$ superlattices and single-unit-cell-thick $SrRuO_3$ samples that are capped with $SrTiO_3$. We achieve samples of exceptional quality. In these samples, the electron systems comprise only a single RuO_2 plane. We observe conductivity down to 50 mK, a ferromagnetic state with a Curie temperature of 25 K, and signals of magnetism persisting up to approximately 100 K.

DOI: 10.1103/PhysRevX.9.011027

Subject Areas: Condensed Matter Physics, Magnetism, Strongly Correlated Materials

I. INTRODUCTION

The creation of an atomically thin ferromagnetic and conducting electron system has been a long-standing goal in science. If realized, it will combine the advantages of two-dimensional electron systems with those of magnetic materials, i.e., state control by electric and magnetic fields. Atomically thin transition-metal films can remain ferromagnetic [1–4], but these electron systems are stable only in a vacuum, limiting their impact. Moreover, these electron systems are not electrically isolated, because the substrates are metallic. Similarly, ferromagnetism has also been observed in hydrogen-doped graphene grown on graphite [5] or at single hydrogen adatoms on graphene [6]. Recently, ferromagnetism has been observed in isolated atomically thin van der Waals crystals of CrI_3 [7], bilayer van der Waals crystals of $Cr_2Ge_2Te_6$ [8], and epitaxially grown van der Waals crystals of $MnSe_2$ [9]. The small size of most of the van der Waals crystals, however, hampers the investigation of these materials, and, e.g., measurements of the electrical conductivity are challenging. Transition-metal-oxide heterostructures circumvent these issues of stability [10] and crystal size and can be grown on insulating substrates, thus realizing isolated electron systems that can be electrically contacted and controlled. Most magnetic and conducting transition-metal-oxide materials, however, lose their functional properties well before the single-unit-cell layer thickness is reached; typically, a nonconducting and nonmagnetic dead layer is present [11–16].

$SrRuO_3$ is one of the oxide materials with the highest conductivity, and it is chemically inert. Therefore, it is widely used in applications such as electrodes of capacitors [17,18]. In addition, it is an itinerant ferromagnet with a saturation moment of 1.6 μ_B/Ru and a Curie temperature T_C of 160 K [19]. Band-structure calculations reveal a 1-eV Stoner splitting of the majority and minority spin bands, resulting in a 60% majority spin polarization [20]. As $SrRuO_3$ has low intrinsic disorder and its epitaxial growth is well understood [21–23], it is a good candidate for realizing a two-dimensional spin-polarized electron system.

Several studies have investigated the behavior of ultrathin $SrRuO_3$ films and $SrRuO_3$ superlattices [24–32]. In most studies, however, an insulating state is observed when the $SrRuO_3$ thickness is less than three unit cells. Additionally, this insulating state has been proposed to be antiferromagnetic [28]. Several theoretical studies agree

*Present address: School of Physical and Mathematical Sciences and School of Electrical and Electronic Engineering, Nanyang Technological University, Singapore 637371, Singapore.

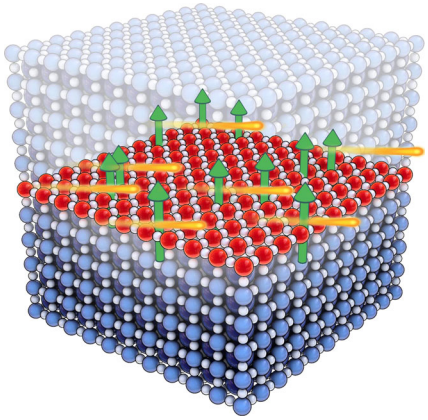

FIG. 1. Schematic of a $SrRuO_3$ layer embedded in $SrTiO_3$. The electron system of the $SrRuO_3$ layer comprises a single RuO_2 plane.

with the antiferromagnetic and insulating ground state in ultrathin $SrRuO_3$ [33,34]. Nonetheless, one theoretical study concludes that ferromagnetism remains down to two-unit-cell-thick layers. In that work, films with a thickness of only one unit cell are predicted to be nonferromagnetic owing to surface-driven effects [35]. Based on this reasoning, these surface effects ought to be nonexistent in $SrTiO_3 - SrRuO_3$ superlattices. Indeed, it has been proposed that a one-unit-cell-thick $SrRuO_3$ layer, i.e., a single RuO_2 plane, remains metallic and is fully minority spin polarized if embedded in a $SrTiO_3$ lattice (Fig. 1) [36,37]. According to that proposal, the octahedral structure of the atomically thin $SrRuO_3$ is stabilized by structural coupling to the $SrTiO_3$ [36]. Recent experiments indeed show an enhancement of the T_C by capping the $SrRuO_3$ with $SrTiO_3$ [38]. To test whether one-unit-cell-thick $SrRuO_3$ is indeed magnetic and conducting if embedded with $SrTiO_3$ in a heterostructure, we fabricate high-quality $(SrRuO_3)_1 - (SrTiO_3)_5$ superlattices and single-unit-cell-thick $SrRuO_3$ samples that are capped with $SrTiO_3$. These layers exhibit conductivity and ferromagnetism, in support of the proposal that for this atomically thin electron system a ferromagnetic ground state can be stabilized.

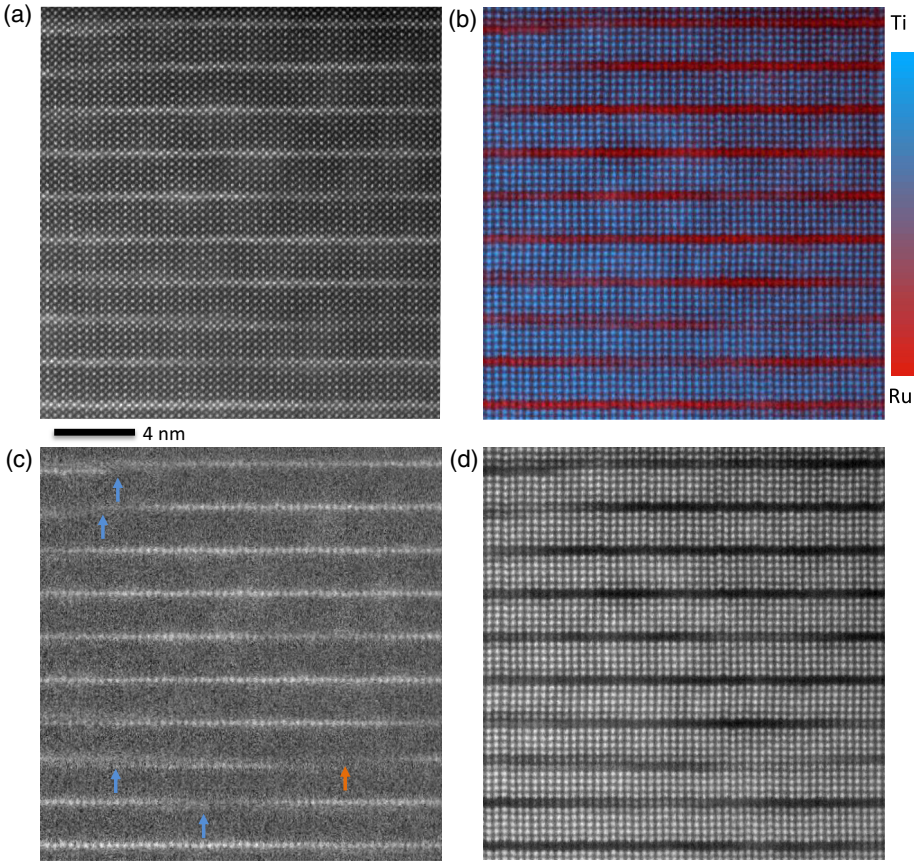

FIG. 2. Scanning transmission electron micrographs of the $(SrRuO_3)_1 - (SrTiO_3)_5$ superlattice sample *B*. In (a) is the simultaneous HAADF image acquired during the spectroscopic acquisition. (b) A color overlay of the titanium and ruthenium signals, with titanium in blue and ruthenium in red, as shown on the color bar. (c) The ruthenium map from the $M_{4,5}$ edge and (d) the titanium map from the $L_{2,3}$ edge. The maps show the film is well ordered with a clear separation of the $SrRuO_3$ and $SrTiO_3$ layers. Blue arrows show locations of step edges, and the orange arrow shows a location where the ruthenium might be discontinuous in this projection.

II. SAMPLE GROWTH AND STRUCTURAL CHARACTERIZATION

The $(SrRuO_3)_1 - (SrTiO_3)_5$ superlattices are grown by reactive molecular-beam epitaxy (MBE) on (001) $SrTiO_3$ substrates, using the growth parameters listed in the Appendix. MBE enables excellent ruthenium stoichiometry control, including the minimization of ruthenium vacancies, the crucial ingredient for high-quality $SrRuO_3$ layers [39]. Superconducting films of the closely related compound Sr_2RuO_4 with the highest transition temperature are also achieved by MBE [40]. For our samples, the growth parameters are optimized such that the correct ruthenium stoichiometry is obtained in thick films, as evidenced by the high residual resistivity ratio of 40 [41]. In independent deposition runs, we fabricate two $(SrRuO_3)_1 - (SrTiO_3)_5$ superlattice samples *A* and *B*, both of which have 20 repetitions of the building blocks. Furthermore, we grow a sample *C* that consists of a single unit-cell-thick layer of $SrRuO_3$ capped with 20 unit cells of $SrTiO_3$.

We analyze the sample structure of the superlattices with scanning transmission electron microscopy (STEM) using both high-angle annular dark-field (HAADF) and electron-energy loss spectroscopy (EELS) imaging. Details of the EELS analysis are provided in Supplemental Material [42]. A representative image of sample *B* is shown in Fig. 2. Figure 2(a) shows the simultaneous annular dark-field image, Fig. 2(b) shows the ruthenium (red) and titanium (blue) color overlay, and Figs. 2(c) and 2(d) show the ruthenium and titanium signals, respectively. The ruthenium map and titanium map show that ruthenium is confined to single, two-dimensional layers. In this large field of view, step edges are apparent in the film [blue arrows in Fig. 2(c)]. Step edges are present in even in the best substrates, and, when the epitaxial film is deposited, the step edges form atomic-scale terraces and the step edges propagate up in the thin film. Often, these step edges run at angles through the film that are not parallel to the direction of the electron beam, so in the projection image of the thin sample we may see two partial layers of lower-intensity ruthenium. In this way, one single layer of ruthenium deposited over a step edge may appear in a projection image as an overlapping area with two $SrRuO_3$ layers with lower intensity. Because there is only one ruthenium layer shared between two rows, the HAADF and EELS ruthenium intensity near the step edges will be reduced compared to the single ruthenium layer. We observe this difference in the HAADF and EELS maps [Figs. 2(a) and 2(c), blue arrows]. Additionally, the titanium signal is also present but less intense in these partial ruthenium layers [Fig. 2(d)]. If two layers of ruthenium were present, the ruthenium intensity in both layers would be the same as that of a single layer, and we would expect no titanium to be present in those layers. We do not see an accumulation of ruthenium forming two layers in this manner, even near the step edges in the

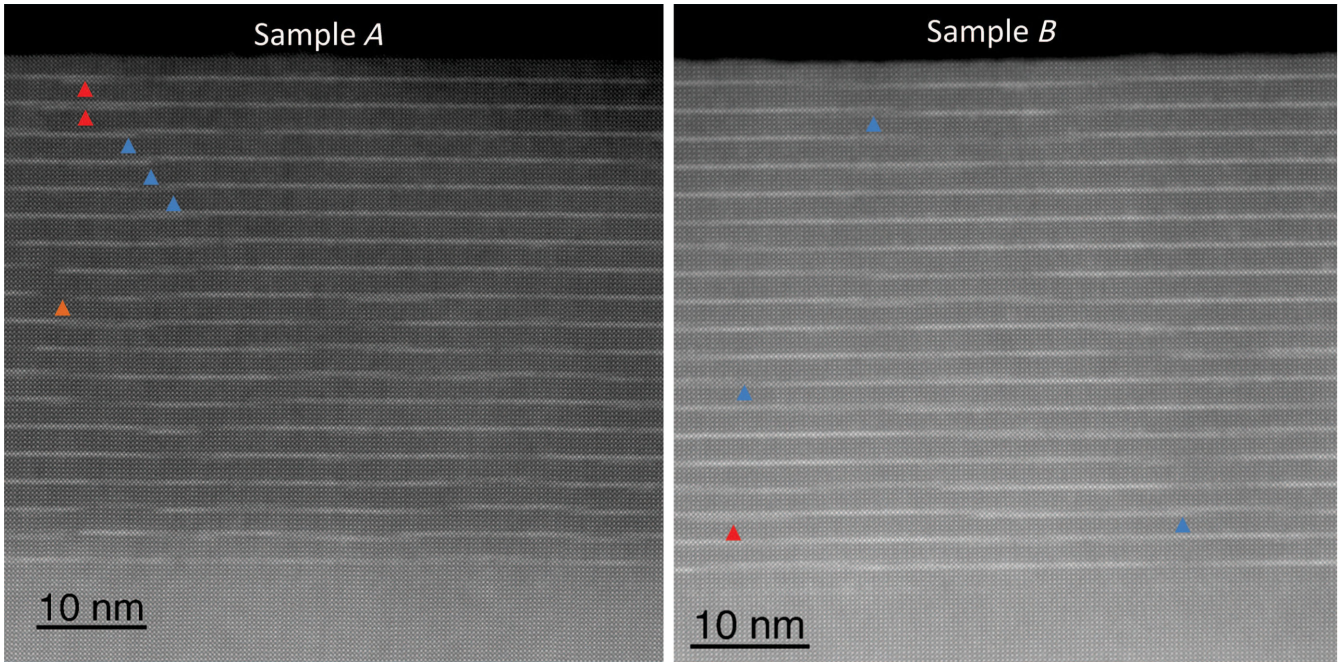

FIG. 3. Lower-magnification HAADF-STEM images of the superlattices. Bright layers of $SrRuO_3$ are seen between five layers of $SrTiO_3$. At the bottom of the images, the $SrTiO_3$ substrates are seen, and the dark layers at the top of the images are epoxy from the TEM sample preparation. Step edges from the substrate are seen propagating through the film (blue arrows), showing 10–60 nm continuous single-layer sheets of ruthenium before encountering a step edge. There are a few regions ($< 0.5\%$) that may contain ruthenium double layers (red arrows) and some regions with discontinuous ruthenium (orange arrow).

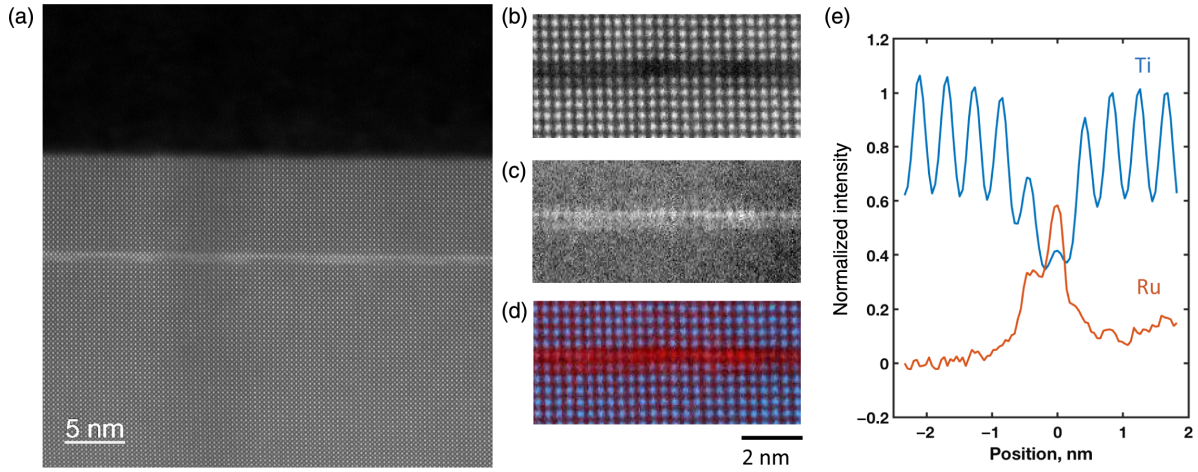

FIG. 4. STEM-EELS of the single-monolayer-thick $SrRuO_3/SrTiO_3$ sample *C*. (a) HAADF STEM image overview. (b) Integrated Ti-$L_{2,3}$ edge, showing significant intensity in the Ru-rich layer. (c) Integrated Ru-$M_{4,5}$ edge processed in a similar manner to the superlattice sample and (d) color overlay of titanium and ruthenium signals. The integrated line profile is shown in (e)—indicating the spread of ruthenium across two unit cells, adding up to 1.2 monolayers of ruthenium.

film. These factors indicate that the ruthenium layers are largely continuous two-dimensional sheets and do not form double ruthenium layers. We also see some regions where the ruthenium layer does not look continuous [orange arrow, Fig. 2(c)].

Larger field-of-view images are shown in Fig. 3 of both samples *A* and *B*. Now we can interpret the HAADF STEM images with our understanding of the structure gained from the EELS spectroscopic images. We see in both samples that, where there are two overlapping layers of ruthenium, the intensity of the ruthenium is typically less and moving over what appears to be a step edge (e.g., see the blue arrows). There are some small regions (red arrows) that do appear to have two ruthenium layers, and, by analyzing several large field-of-view images, in sample *A* there is an upper bound of 0.4% two-layer $SrRuO_3$, and in sample *B* there is an upper bound of 0.3% two-layer $SrRuO_3$. We also find some regions of discontinuous $SrRuO_3$ where there appears to be no ruthenium layer (orange arrow). Because the overwhelming majority of the ruthenium layers are single ruthenium layers, these are remarkably well-ordered superlattices despite the occasional (and inevitable) presence of step edges. For both samples, the $SrRuO_3$ layers are continuous for approximately 10–60 nm before encountering a step edge.

The STEM-EELS analysis of sample *C* is shown in Fig. 4. From the HAADF images, it appears that the $SrRuO_3$ is spread across two unit cells in the structure. This spreading is confirmed by EELS mapping, which shows that a significant fraction of the *B* sites in what is expected to be a ruthenium row are titanium. The ruthenium is spread across one, two, or three layers in projection. By integrating the *B*-site intensity column by column, we find an average ruthenium density of 1.19 ± 0.04 monolayers of ruthenium. This amount is slightly more than the nominal one monolayer that is found in the superlattice samples.

Figure 5 presents x-ray diffraction (XRD) scans of the superlattice samples, exhibiting the expected superlattice reflections at distances $n\delta$ separated from the $SrTiO_3$ Bragg reflections. Here, n is an integer, and δ is the ratio between the lattice parameter of $SrTiO_3$ and the superlattice period. These reflections indicate that the ordering in the samples is macroscopic. Small deviations of the peak positions are observed in sample *B* with respect to the calculated peak positions for a $(SrRuO_3)_1 - (SrTiO_3)_5$ superlattice. These deviations are due to the average $SrTiO_3$ thickness being

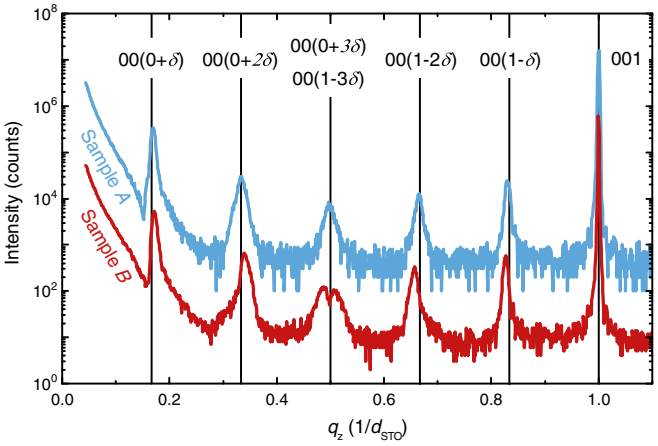

FIG. 5. θ-2θ x-ray diffraction of the $(SrRuO_3)_1 - (SrTiO_3)_5$ superlattices. Out-of-plane scattering scans of samples *A* and *B* showing the $00(0+\delta)$ to $00(0+3\delta)$ and the $00(1-3\delta)$ to $00(1-\delta)$ superlattice reflections and the 001 $SrTiO_3$ Bragg peak. The vertical lines indicate the calculated peak positions for a $(SrRuO_3)_1 - (SrTiO_3)_5$ superlattice. The small deviations of the peak positions in sample *B* are due to the average $SrTiO_3$ thickness being less than five unit cells.

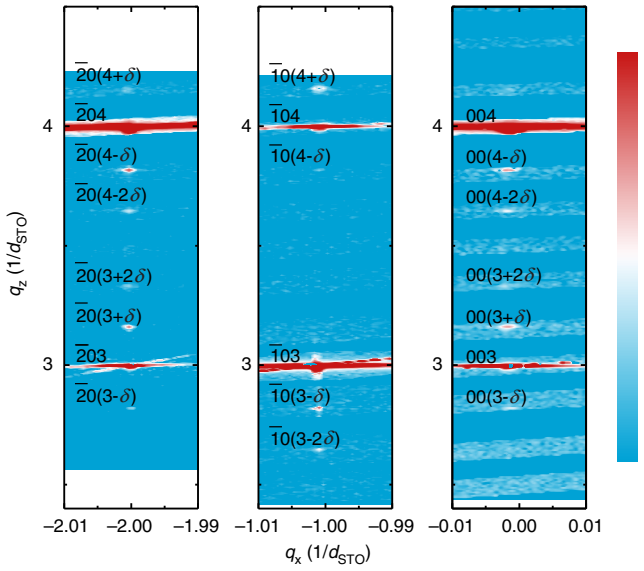

FIG. 6. XRD reciprocal-space maps of sample A. The bright red peaks are the $SrTiO_3$ Bragg reflections. The superlattice peaks are visible as tails below the $SrTiO_3$ peaks and as the white dots in between the $SrTiO_3$ peaks. The color bar denotes the logarithmic intensity scale. The color scale oversaturates the $SrTiO_3$ Bragg peaks in order to better show the weak superlattice reflections. The superlattice reflections are indicated with labels that are placed to the top left of the peaks.

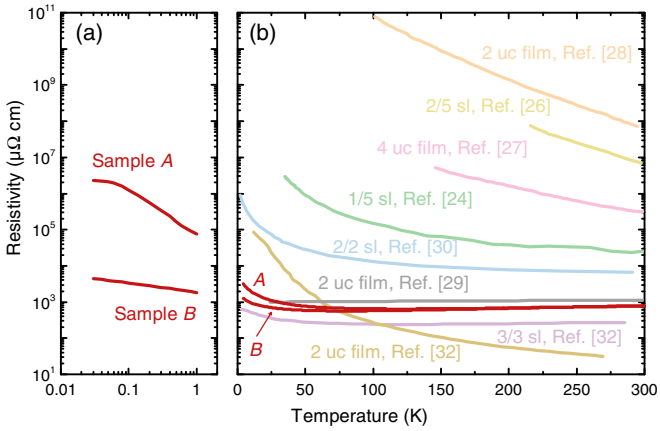

FIG. 7. Temperature dependence of the resistivities of samples A and B. (a) Temperature range below 1 K on a logarithmic scale. (b) Temperature range $2 < T < 300$ K on a linear scale. For comparison, thin-film and superlattice (sl) samples found in the literature with a comparable thickness of the $SrRuO_3$ layers are also shown. The superlattices are $\{(SrRuO_3)_1 - (SrTiO_3)_5\}_{20}$ [24], $\{(SrRuO_3)_2 - (BaTiO_3)_5\}_{36}$ [26], $\{(SrRuO_3)_2 - (LaAlO_3)_2\}_{60}$ [30], and $\{(SrRuO_3)_3 - (SrTiO_3)_3\}_{15}$ [32]. All samples are grown on $SrTiO_3$ substrates.

4.8 unit cells instead of five, and they are not expected to affect the properties of the $SrRuO_3$ layers (Supplemental Material [42]). Furthermore, we also measure reciprocal-space maps of sample A along the $\bar{2}0L$, the $\bar{1}0L$, and the $00L$ lines (Fig. 6). Relatively strong superlattice reflections are found for $3 < L < 4$ along $\bar{2}0L$, for $L < 3$ and for $L > 4$ along $\bar{1}0L$, and for $3 < L < 4$ along $00L$. Here, L is normalized to the $SrTiO_3$ reciprocal lattice. The entire superlattice structure is coherently strained to the lattice parameter of the $SrTiO_3$ substrate. The mosaicity of the superlattice is smaller than 0.05°, as determined from the full width at half maximum of the rocking curves.

III. ELECTRICAL TRANSPORT

The temperature dependence of the resistivity ρ of samples A and B is shown in Fig. 7 together with literature data. In the temperature range between 2 and 300 K, the samples have a resistivity of approximately 1000 $\mu\Omega$ cm, corresponding to a sheet resistance of 25 kΩ for a single $SrRuO_3$ layer. This resistivity is higher than either the bulk or the thick-film resistivity [18] but significantly lower than the resistivities of the two-unit-cell-thick films and the $(SrRuO_3)_{1,2} - (ABO_3)_n$ superlattices of the previous studies [24–30,32]. The decreased resistivity is due partially to the superlattice structure and partially to the high structural quality of our samples. The samples show a minimum of the resistivity at 120 (sample A) and 80 K (sample B); see also Fig. 11(a) for a linear plot of the data. Below these temperatures, $d\rho/dT$ is negative, possibly owing to localization of the charge carriers. To shed light on the ground state of the system, we measure $\rho(T)$ down to 30 mK [Fig. 3(a)]. The resistance of the superlattice samples increases continually with a decreasing temperature, in contrast to the theoretical predictions [36,37]. Nevertheless, a finite conductivity of the order of 10 μS remains at the lowest temperature. In this temperature range, a large difference between the samples is observed. Surprisingly, the sample found by our XRD measurements to have a higher structural quality also has the greater resistance.

To elucidate the presence of the magnetization in the samples, we first study the magnetoresistance (MR). The MR is generally parabolic in nonmagnetic conductors. In the ferromagnetic state of $SrRuO_3$, in contrast, the domain-wall resistance is known to be the dominant contribution to the MR [43]. With an increasing magnetic field, the density of the domain walls is reduced, and, therefore, a decrease of the resistance with an applied magnetic field is expected. Thus, the presence of a negative (nonparabolic) MR is considered to be a strong indication of ferromagnetism. Indeed, for nonmagnetic samples of two- and three-unit-cell thickness, only a very small MR is found [28]. The MR of samples A and B is shown in Figs. 8(a) and 8(b) for perpendicular fields up to 5 T. Above 100 K, hardly any MR is observed, and below 100 K, the MR increases steadily with a decreasing temperature to about 12% at $H = 5$ T. Furthermore, below 25 K, a hysteresis is observed in the curves, revealing the butterfly-loop characteristic of ferromagnetic ordering. The upper limit for the magnetic moment in $SrRuO_3$ is 4 μ_B/Ru corresponding to

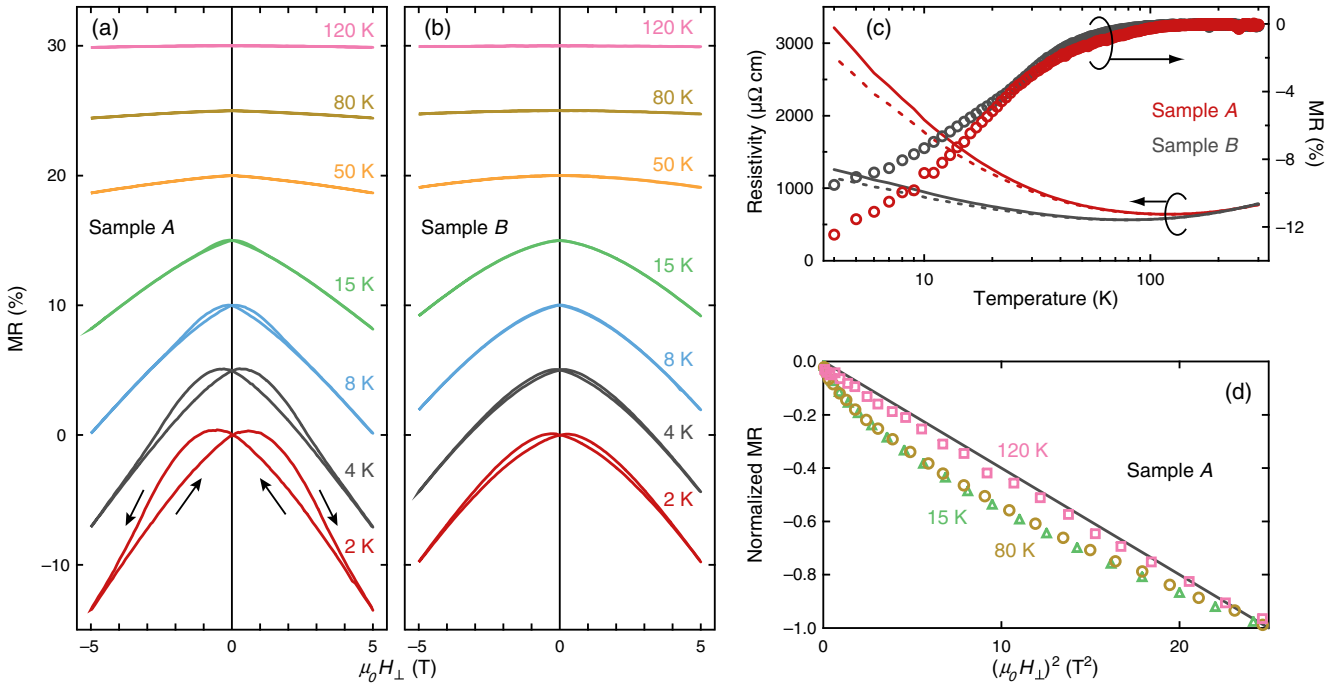

FIG. 8. Magnetoresistance for a perpendicular magnetic field. (a) MR curves at different temperatures for sample *A*. MR sets in below approximately 100 K. At low temperatures, hysteresis is observed in the MR. Arrows denote the direction of the sweep. The MR curves are offset to avoid overlap. (b) Sample *B*. (c) The temperature dependence of the sheet resistance at $H = 0$ T and at $H = 5$ T together with the temperature dependence of the MR $[\rho(0) - \rho(5)]/\rho(0)$. (d) The MR$(H^2)$ dependence of sample *A*. Below 100 K, deviations from the linear behavior are observed. The MR curves are normalized to their values at $H = 5$ T.

a magnetization M of 0.8 T. This value is too small to explain the large hysteresis in the MR by the standard relation $\mathrm{MR} = K(H + M)^2$, where K is an appropriate constant.

Two scenarios can explain the observed MR. In the first scenario, the MR is attributed to the influence of the domain-wall resistance and, accordingly, the hysteresis to domain-wall pinning. Because the MR is observed reversibly in a large magnetic-field range, this model implies that the domain-wall creation energy is small and that pinning sites with varying trapping energies exist. In the second scenario, we have to assume that the samples phase separate into well-conducting ferromagnetic regions and poorly conducting nonmagnetic regions [44]. Then, the transport between the ferromagnetic regions depends on the relative orientation of the magnetic moments in the regions. A hysteresis in the MR results when the different regions reverse their magnetic moments at different values of the magnetic field. In this scenario, the negative $d\rho/dT$ at a low temperature can be explained if the transport between the ferromagnetic regions is dominated by thermally activated hopping. Both scenarios require the presence of ferromagnetism in the samples. The larger hysteresis is observed in sample *A*, the sample with the higher resistivity. This result is consistent with both scenarios: more domain-wall pinning due to an increased number of point defects and/or more electronic inhomogeneity resulting in a larger spread in switching fields. This understanding implies that the temperature at which the hysteresis disappears can be lower than T_C, because that is merely the temperature at which thermal fluctuations exceed the domain-wall pinning or switching field distribution.

We next study the temperature dependence of the MR in greater detail. Figure 8(c) presents the temperature dependence of the resistivity at $H = 0$ T, the resistivity at $H = 5$ T, and the MR $[\rho(0) - \rho(5\ \mathrm{T})]/\rho(0)$. Even though the resistivities of our two samples are different in magnitude, their MRs show similar temperature dependence. The MR at $H = 5$ T is 10%–12% at 4 K and disappears at approximately 100 K, close to the phase-transition temperature of $SrTiO_3$. The MR due to domain-wall resistance and due to an inhomogeneous ferromagnetic network is expected to deviate from parabolic behavior [43,44]. We therefore plot the MR in Fig. 8(d) as a function of H^2. At 120 K, the MR has a linear MR(H^2) dependence; however, below 100 K, pronounced deviations from the linear behavior are observed, especially at small applied fields. We conclude that signatures of magnetism persist in the samples up to a temperature of approximately 100 K.

We also perform measurements on samples *A* and *B* in perpendicular magnetic fields up to 10 T at $T = 500$ and 200 mK (Fig. 9). The samples show a large negative MR (about 30% at $H = 10$ T) with a hysteresis loop that is very similar to the loops observed at higher temperatures.

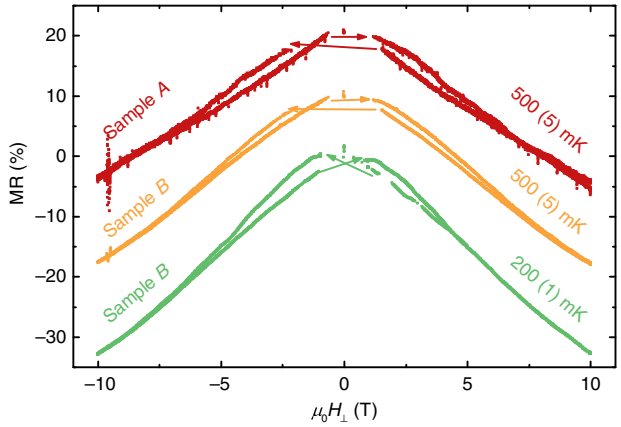

FIG. 9. Magnetoresistance at low temperatures in a perpendicular magnetic field. Large hysteretic magnetoresistance is observed. Because of heating of the samples, the data at low fields are unreliable and are therefore not shown. Arrows indicate the sweep directions. The sweep at 200 mK started at $H = 5$ T instead of $H = 10$ T.

The loops, however, close at higher fields, indicating an increase of the coercive field. We have not observed a saturation of the MR, even at fields of $H = 10$ T. The observation of hysteretic MR at temperatures below 1 K, where the resistivity is orders of magnitude larger, suggests that the second scenario as discussed above (electronic inhomogeneity) is dominant at low temperatures, because it is quite unlikely that the domain-wall resistance has the same temperature dependence as the resistivity.

In addition to the magnetoresistance measurements in a perpendicular field shown in Fig. 8, we measure the magnetoresistance of samples A and B in a parallel field. The data are shown in Fig. 10. Both samples A and B show magnetoresistance below 100 K, just as in the case of the perpendicular magnetic field. A difference in the shape of the MR curves is, however, observed [Figs. 8(a) and 8(b) and Figs. 10(a) and 10(b)]. The in-plane MR is larger, especially at a small field strength. This result is attributed to the magnetocrystalline anisotropy of $SrRuO_3$ thin films. The magnetic easy axis is estimated to be about 10°–15° away from the out-of-plane direction [28]. Therefore, the switching of the in-plane component of the magnetization has a smaller energy barrier than the switching of the out-of-plane component, resulting in stronger low-field MR. Furthermore, no hysteresis is observed in the parallel field. This result is another direct consequence of the smaller energies involved in the switching of the in-plane component of the magnetization. At a large magnetic-field strength, however, the out-of-plane MR and the in-plane MR are similar. The temperature dependence of the MR shows a similar trend for in-plane and out-of-plane magnetic fields [Figs. 8(c) and 10(c)], except for the two-step behavior seen in sample B for an in-plane magnetic field.

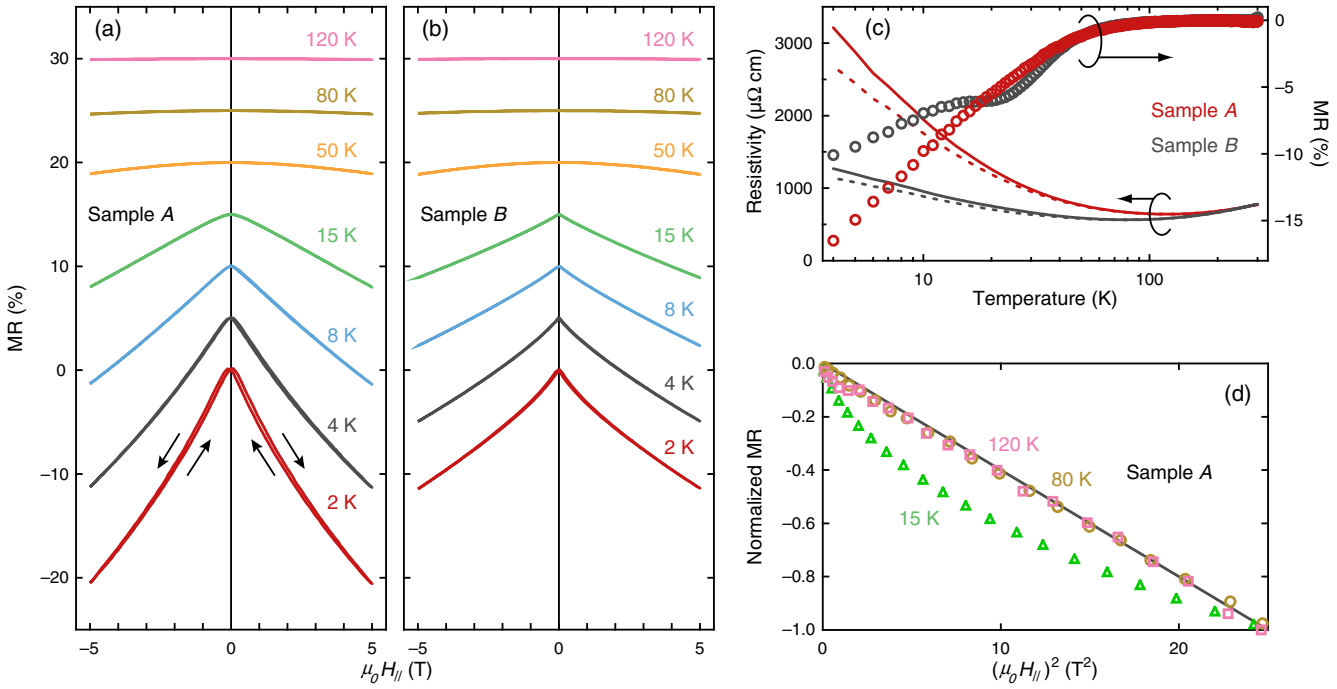

FIG. 10. Magnetoresistance for a parallel magnetic field. (a) MR curves at different temperatures for sample A. The magnetic field is applied parallel to the sample surface. Arrows denote the direction of the sweep. The MR curves are offset to avoid overlap. (b) MR curves for sample B. (c) The temperature dependence of the sheet resistance at $H_{||} = 0$ T and at $H_{||} = 5$ T together with the temperature dependence of the MR $[\rho(0) - \rho(5)]/\rho(0)$. (d) The MR$(H^2)$ dependence of sample A. Below 80 K, deviations from linear behavior are observed. The MR curves are normalized to their values at $H = 5$ T.

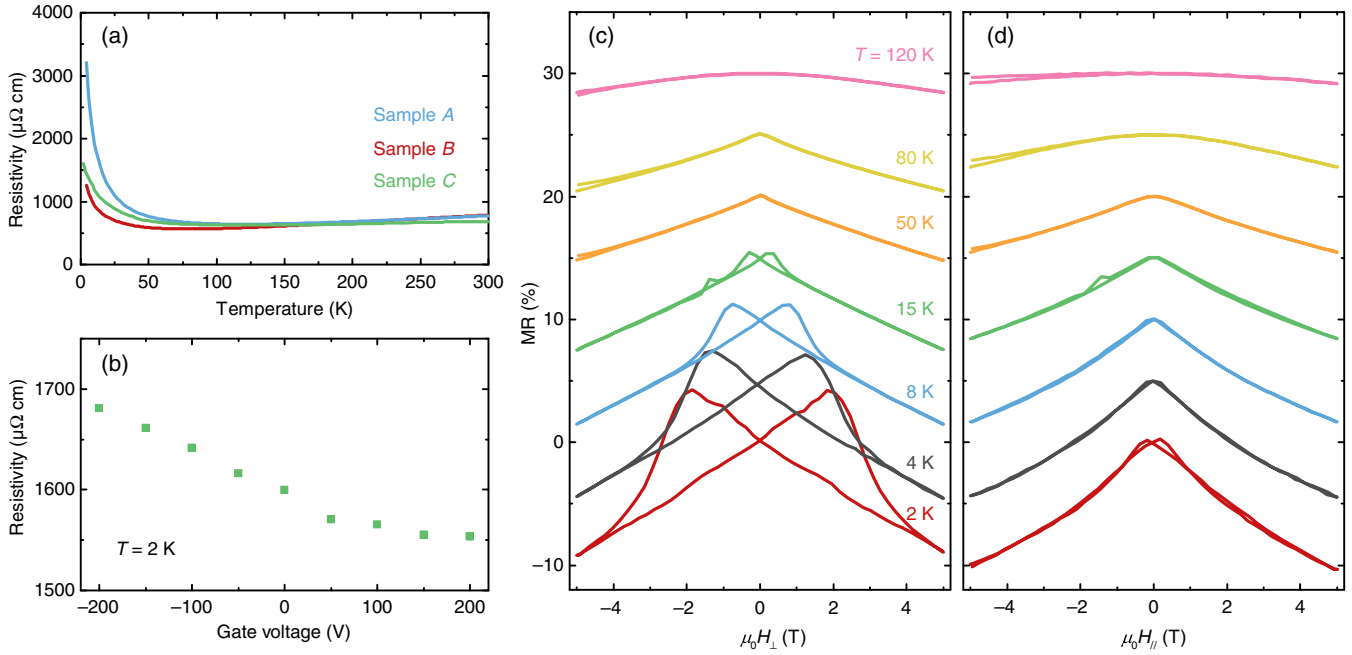

FIG. 11. Resistivity and magnetotransport of sample *C*. (a) Comparison of the temperature dependence of the resistivity between samples *A*, *B*, and *C*. (b) Electrostatic field-effect-dependent resistivity of sample *C* using a back gate. (c) Out-of-plane magnetoresistance. The MR curves are offset to avoid overlap. (d) In-plane magnetoresistance.

The latter is probably due to sample inhomogeneity. The MR(H^2) plot for an in-plane magnetic field is shown in Fig. 10(d). A deviation from linear behavior is observed below 80 K, suggesting that ferromagnetic effects are governing the MR, consistent with the data for the out-of-plane magnetic field shown in Fig. 8(d).

The temperature dependence of the resistivity of sample *C* is shown in Fig. 11(a) together with the data from samples *A* and *B*. The resistivity of sample *C* has a similar temperature dependence as the other samples, and it is of similar magnitude. We investigate the possibilities of electrostatically modifying the sample using a back gate across the 1-mm-thick $SrTiO_3$ crystal. The low-temperature resistivity is modified about 10% by applying positive and negative voltages of up to 200 V [Fig. 11(b)]. The magnetotransport is shown in Figs. 11(c) and 11(d). The low-temperature magnetoresistance is 10% at $H = 5$ T, a butterfly loop is observed for $T \leq 15$ K when the field is applied perpendicular to the layer, and the magnetoresistance deviates from the standard parabolic dependence for $T < \sim 100$ K. These results agree well with the magnetotransport of the superlattice samples. The application of the electrostatic potential does not change the shape and temperature dependence of the out-of-plane magnetotransport characteristics, indicating that the modification of the carrier density is too small to affect the ferromagnetic properties of the sample. We expect that larger changes in the sample properties can be achieved by using thinner gate dielectrics and electrolyte gating.

IV. MAGNETIZATION MEASUREMENTS

We now turn to direct magnetization measurements of the samples. The magnetocrystalline anisotropy of $SrRuO_3$ favors a predominantly out-of-plane magnetic moment for thin films [28]. Therefore, magnetic domain formation is expected to occur, resulting in a reduction of the global possible magnetic moment compared to that of a monodomain sample. The MR data also indicate that the samples are not monodomain. As the anisotropy field is very large, it is difficult to saturate the moment. This difficulty makes conventional magnetization measurements challenging.

We therefore use scanning superconducting-quantum-interference-device (SQUID) microscopy (SSM), which is a very sensitive local measurement technique that can directly image the magnetic domain structure [45,46]. Representative scans of samples *A* and *B* are shown in Figs. 12(a) and 12(b). A magnetic contrast is observed consisting of up and down domains in a bubblelike pattern, consistent with the expected out-of-plane anisotropy. The typical feature size of the magnetic flux pattern is 5–10 μm. The measured magnetic flux corresponds to a magnetic signal of 0.001–0.01 μ_B/Ru in the superlattice, which is much smaller than the theoretical prediction [36] of a fully spin-polarized material. Because the area of the pickup loop is 3×5 μm^2, any possible submicrometer domain structures are averaged out during the measurements. In addition, as the domain structure is not expected to be uniform across the stack of 20 magnetic layers, the

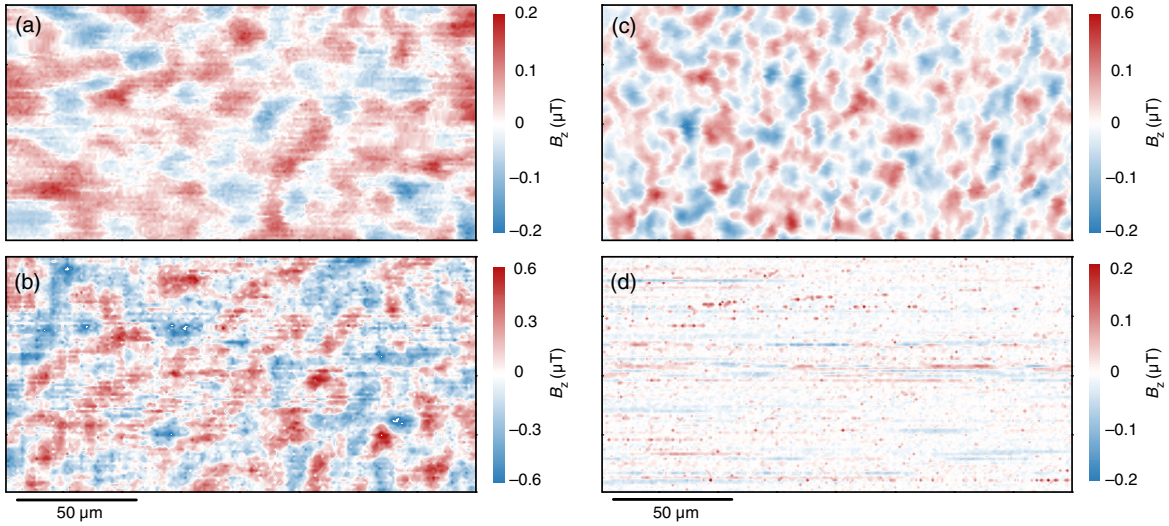

FIG. 12. Scanning SQUID microscopy magnetic signal of samples A (a), B (b), and C (c) measured at $H = 0$ T and $T = 4.2$ K. A ferromagnetic domain pattern is observed. (d) Measurement of a bare $SrTiO_3$ sample. No magnetic signal is observed, indicating that the magnetic signal in the superlattice sample is not due to impurities in the $SrTiO_3$.

measured magnetic signal is smaller than the magnetic moment inside the domains.

Figure 12(c) shows the magnetization as imaged by scanning SQUID microscopy of sample C. A domain pattern is found that agrees well with the domain patterns observed in the superlattice samples. The magnitude of the magnetic signal corresponds to approximately 0.2 μ_B/Ru, which is much larger than the moment observed in the superlattice samples. This result indicates that the magnetization in the different layers in the superlattice samples partially cancels out. For reference, a $SrTiO_3$ sample is imaged as well. A $SrTiO_3$ layer of 100 unit cells is grown using identical settings as the $SrTiO_3 - SrRuO_3$ superlattices. No magnetic signal is observed [Fig. 12(d)], indicating that the magnetic signal in the $SrRuO_3$ samples is not due to impurities in the $SrTiO_3$. Note that SSM detects only ferromagnetism from the surface of the sample, eliminating possible contributions from the back side of the sample. The magnetic domain patterns observed in samples A, B, and C clearly proves the samples to be ferromagnetic.

Additionally, we perform magnetic torque and magnetization measurements on the superlattice samples. Magnetic torque, $\tau = \mu_0 M \times H$, is sensitive only to anisotropic magnetic responses. Figure 13 shows torque curves obtained from the superlattice samples, together with the magnetic hysteresis loops obtained from the torque data. In these measurements, positive torque corresponds to a net magnetic moment in the in-plane direction and negative torque to a net magnetic moment in the out-of-plane direction when the magnetization is aligned with the projection of the field. Both samples show strong hysteretic behavior, characteristic of ferromagnetic ordering. As discussed in detail in the previous section, the magnetic anisotropy of $SrRuO_3$ favors a domain structure in which the magnetization vector is rotated away from the out-of-plane direction. This domain structure can generate a net magnetic moment in both the in-plane and the out-of-plane directions, depending on the volume fractions of the different domains. The magnetic hysteresis loop of sample A contains two contributions: an in-plane magnetic hysteresis with a switching field of $H = 4$ T and an out-of-plane contribution that is linear in field and saturates above $H = 3$ T. The saturation moments are 0.08 and 0.04 μ_B/Ru for the in-plane and out-of-plane components, respectively. The magnetic hysteresis loop of sample B, in contrast, contains an out-of-plane hysteretic component and a linear, nonsaturating, in-plane component. The saturation magnetization of the out-of-plane component is 0.05 μ_B/Ru. With an increasing temperature, the switching fields are reduced, and, for $T > 25$ K, the samples are no longer hysteretic. A smaller magnetic signal, however, persists up to higher temperatures (Supplemental Material [42]). As discussed in detail in Supplemental Material [42], the observed difference between the samples is attributed to the complicated magnetic domain structure and variations in domain pinning strength that affect the switching field distributions. We find that the saturation moment varies for different pieces of the samples between approximately 0.05 and 0.5 μ_B/Ru (Supplemental Material [42]). The torque measurements clearly show the atomically thin $SrRuO_3$ layers to have a spontaneous magnetization and, therefore, to be ferromagnetic. The magnetic moment is too large to be explained by the small number of two-unit-cell-thick $SrRuO_3$ areas in the samples. Both the disappearance of the magnetic hysteresis at $T \approx 25$ K and the observation of a magnetic signal for $T > 25$ K are in good agreement with the MR data.

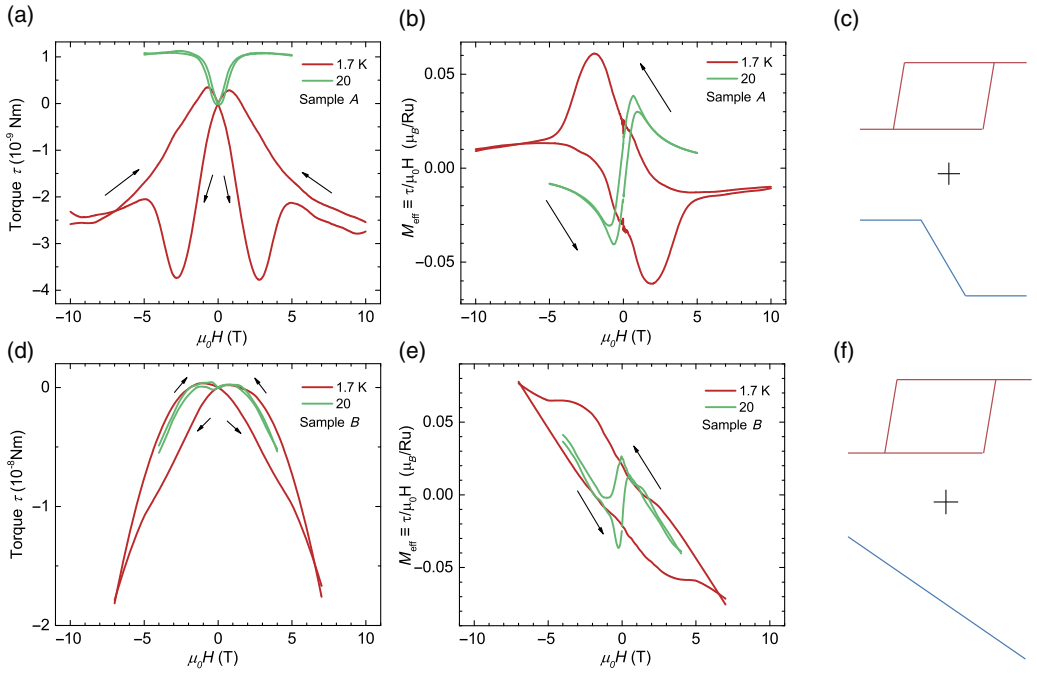

FIG. 13. Torque magnetometry. (a) Torque measured as a function of the applied field at different temperatures for sample *A*. The magnetic field is applied 70° away from the surface normal. (b) The corresponding magnetization (field) characteristics. Here, the projected magnetization τ/H is shown; to obtain the actual magnetization values, the data should be divided by sin(20°) or by sin(70°) for the in-plane and out-of-plane contributions, respectively. (c) The sketch shows the two contributions to the magnetic signal: the in-plane hysteresis loop (red) and the out-of-plane linear contribution that saturates at high fields (blue). (d)–(f) The same for sample *B*.

V. CONCLUSIONS

In conclusion, we have shown atomically thin $SrRuO_3$ to be ferromagnetic and conducting if embedded in $SrTiO_3$. The observation that conductivity and ferromagnetism is present in both the superlattices and in the single-layer sample indicates that the magnetization and conductivity originates from the properties of atomically thin layers of $SrRuO_3$ and do not arise because of coupling between the layers. In these samples, the electron systems comprise only a single RuO_2 plane. Magnetic hysteresis is observed for $T < 25$ K, and signals of magnetism persist up to approximately 100 K. Because the observed magnetic moment is only 3%–30% of the magnetic moment of bulk $SrRuO_3$, we cannot exclude an inhomogeneous electron system with magnetic and nonmagnetic areas. These structures are a rare example of two-dimensional ferromagnetism and the first demonstration of two-dimensional ferromagnetism due to indirect exchange. They may therefore serve as a model system for further theoretical studies [4]. The conductance and T_C of atomically thin $SrRuO_3$ is expected to increase with additional charge carrier doping [47], possibly resulting in a triplet superconducting ground state [48]. With recent advances in electric-field gating technology [49–51], we expect electric-field control of the conductivity and ferromagnetism to become possible.

ACKNOWLEDGMENTS

We gratefully acknowledge discussions with and support from E. Benkiser, M. Fiebig, P. Garcia-Fernández, T. Günter, J. Junquera, G. Khalliulin, B. Keimer, T. Kopp, C. Richter, J. Smet, A. Schmehl, M. Randeria, and F. S. Wells. Furthermore, we thank J. Junquera and P. Garcia-Fernández for triggering this work. The work at Cornell was supported by the National Science Foundation (NSF) through the MIP program [Platform for the Accelerated Realization, Analysis, and Discovery of Interface Materials (PARADIM)] under Cooperative Agreement No. DMR-1539918 and was performed in part at the Cornell NanoScale Science & Technology Facility (CNF), a member of the National Nanotechnology Coordinated Infrastructure (NNCI), which is supported by the National Science Foundation (Grant No. ECCS-1542081). Electron microscopy by M. E. H. was supported by the U.S. Department of Energy, Office of Basic Energy Sciences, Division of Materials Sciences and Engineering under Award No. DE-SC0002334. This work made use of the electron microscopy facility of the Cornell Center for Materials Research with funding from the NSF MRSEC program (DMR-1719875). M. E. H. thanks M. Thomas, J. Grazul, and J. Mundy for assistance in the microscope facilities. X. R. W. thanks the Dutch NWO-Rubicon Grant [No. 2011, 680–50–1114] for financial support. The torque magnetometry work at Michigan was supported by the U.S.

Department of Energy (DOE) under Award No. DE-SC0008110.

A. S., H. N., and C. R. H. prepared the samples. D. G. S. supervised the sample growth. C. R. H., T. H., and H. B. performed the transport measurements. M. E. H. and D. A. M. performed the electron microscopy, and X. R. W., P. R., and H. H. performed the scanning SQUID microscopy. T. A., L. L., and R. A. performed the torque magnetometry and A. V. B. the muon spin rotation experiments. J. M. supervised the research. H. B., C. R. H., T. H., and J. M. wrote the manuscript. All authors contributed to the discussion and provided feedback on the manuscript.

APPENDIX: METHODS

$SrRuO_3 - SrTiO_3$ superlattices are deposited with MBE on TiO_2-terminated (001) $SrTiO_3$ substrates at 680 °C using shuttered deposition of the elements Ti, Sr, and Ru. Reflection high-energy electron diffraction (RHEED) oscillations are monitored to determine the deposition time. The samples are grown in a distilled ozone atmosphere of 6.7×10^{-7} mbar. After growth, the samples are cooled to room temperature over the course of one hour under the same ozone pressure in which they are grown. For the single-layer samples, we grow one monolayer of $SrRuO_3$ capped with 20 unit cells of $SrTiO_3$ at a substrate temperature of 680 °C and a chamber background pressure of 1.1×10^{-6} Torr (of approximately 10% O_3 + 90% O_2) on (001)-oriented $SrTiO_3$ substrates. The temperature is measured with a pyrometer at a measurement wavelength of 980 nm that detects the temperature of the platinum adhesion layer on the back side of the substrate. We obtain a singly terminated substrate surface by thermal annealing at 1300 °C [52]. The one-monolayer-thick $SrRuO_3$ is grown in an adsorption-controlled regime, where the excess ruthenium evaporates off the film surface as RuO_x ($x = 2$ or 3) [23]. Strontium is evaporated from a low-temperature effusion cell, titanium flux is provided by a Ti-Ball™ source [53], and ruthenium is evaporated from an electron beam evaporator. Before growth, the strontium and titanium fluxes are calibrated to an uncertainty of less than 1% using shuttered RHEED oscillations [54], while the ruthenium flux is calibrated using a quartz crystal microbalance (QCM). Postgrowth, the samples are cooled down below 100 °C under the same ozone pressure in which they are grown.

Cross-sectional STEM specimens are prepared either by mechanical wedge polishing followed by Ar-ion milling [55] (sample *A*) or by focused ion beam (FIB) lift-out (samples *B* and *C*). FIB lift-out is performed using an FEI Strata 400 FIB with a final milling step of 2 keV to reduce surface damage. STEM and EELS data are recorded from cross-sectional specimens in the 100-keV NION UltraSTEM, a fifth-order aberration-corrected microscope optimized for EELS spectroscopic imaging with a probe size of approximately 1 Å, an EELS energy resolution of 0.4 eV, and a beam current of 100–200 pA. Large spectroscopic maps of the Ru-$M_{4,5}$ edge and the Ti-$L_{2,3}$ edge are acquired with an energy dispersion of 0.25 eV/channel with a Gatan Quefina dual-EELS spectrometer. For the large spectroscopic images, we integrate components of the spectra over energies corresponding to ruthenium and titanium after a linear combination of power-law background subtraction. Because of the close proximity of the Sr-$M_{2,3}$ and Ru-$M_{4,5}$ edges, and the Ru-$M_{2,3}$ and Ti-$L_{2,3}$ edges, we use small integration windows and principal component analysis (PCA) filtering to remove noise, keeping the six components of the spectra which capture all of the spatially varying components. The ruthenium is extracted from the tail of the $M_{4,5}$ edge, and the titanium is extracted from the first 1.5 eV of the Ti edge. To ensure PCA is returning no artifacts, we also use dual EELS to simultaneously map the Ru-$L_{2,3}$ edge and the Ti-$L_{2,3}$ edge, shown in Supplemental Fig. S1 [42]. The high energy of the Ru-$L_{2,3}$ edge makes it prohibitive to do large spectroscopic maps shown in the main text, although the mapping with the Ru-$M_{2,3}$ edge provides qualitatively similar results.

The resistivity measurements for $T < 1$ K are performed using a He^3/He^4 dilution refrigerator and a low-frequency ac lock-in measurement technique with a 1-nA excitation. The high resistivity of sample *A* makes the measurements problematic. We do therefore not obtain reliable data of the magnetotransport of this sample at $T = 200$ mK. It turns out that the temperature of the samples is not stable at low fields due to the relatively high sweep rates of the magnetic field used during the experiment. We attribute the thermal instability to magnetocaloric parts in the sample holder. The temperature varies up to 25 mK, and, since the samples have a strong temperature dependence of the resistivity in this temperature range, an error is made in the magnetoresistance measurements. We therefore exclude all data where the temperature is outside of a window of 2 (for the 200-mK sweep) and 10 mK (for the 500-mK sweep) from the analysis. We note that these temperature fluctuations do not affect the magnetic structure inside the samples. The resistivity and MR measurements for $T > 2$ K are performed with a Quantum Design physical properties measurement system using a 20 μA dc current excitation. The transport measurements determine the sheet resistance R_{sheet} of the samples. The resistivity ρ of the samples is obtained from the sheet resistance by $\rho = R_{\mathrm{sheet}} \cdot d$. Here, d is the total thickness of the conducting layer(s) that corresponds to either 20 times approximately 0.4 nm (samples *A* and *B*) or approximately 0.4 nm (sample *C*).

The SSM measurements are performed using a square pickup loop with an inner dimension of approximately 3×5 μm^2. During the measurement, the pickup loop is scanned approximately 2 μm above the sample surface at a contact angle of approximately 10°. The SSM records the variation of magnetic flux threading the pickup loop,

and the flux detected by the pickup loop is converted to a magnetic field by dividing by the effective pickup area of approximately 15 μm^2. The typical flux sensitivity of the SSM is around 14 $\mu\Phi_0 Hz^{-1/2}$, where $\Phi_0 = 2 \times 10^{-15}$ T m^2 is the flux quantum and the bandwidth is 1000 Hz. As our SSM sensor has a 10-degree inclination, the measured magnetic stray-field component B_z is almost perpendicular to the sample surface. The practical sensitivity during measurements is set by external noise sources and is estimated to be about 30 nT.

We perform torque magnetometry measurements with a homebuilt cantilever setup by attaching the samples to a thin beryllium copper cantilever. Under an external magnetic field H, the sample rotation is measured by tracking the capacitance between the metallic cantilever and a fixed gold film underneath using an AH2700A capacitance bridge with a 14-kHz driving frequency. To calibrate the spring constant of the cantilever, we track the angular dependence of the capacitance caused by the sample weight at a zero magnetic field.

We also explore the magnetization in the samples by SQUID measurements and by muon spin rotation. In these experiments, no (muon spin rotation) or only a weak (SQUID) magnetic signal is observed beyond the diamagnetic background of the $SrTiO_3$ substrate. It is not possible to attribute the magnetic signal observed in the SQUID measurements to a signal originating in the $SrRuO_3$, because the signal could also arise from impurities in the $SrTiO_3$. Therefore, we discuss only the magnetoresistance, SSM, and torque measurements here.

[1] R. Pfandzelter, G. Steierl, and C. Rau, *Evidence for* 4*d Ferromagnetism in 2D systems: Ru Monolayers on C(0001) Substrates*, Phys. Rev. Lett. **74**, 3467 (1995).

[2] P. Gambardelli, A. Dallmeyer, K. Maiti, M. C. Malagoli, W. Eberhardt, K. Kern, and C. Carbone, *Ferromagnetism in One-Dimensional Monatomic Metal Chains*, Nature (London) **416**, 301 (2002).

[3] J. Shen and J. Kirshner, *Tailoring Magnetism in Artificially Structured Materials: The New Frontier*, Surf. Sci. **500**, 300 (2002).

[4] C. A. F. Vaz, J. A. C. Bland, and G. Lauhoff, *Magnetism in Ultrathin Film Structures*, Rep. Prog. Phys. **71**, 056501 (2008).

[5] A. J. M. Giesbers, K. Uhlirova, M. Konecny, E. C. Peters, M. Burghard, J. Aarts, and C. F. J. Flipse, *Interface-Induced Room-Temperature Ferromagnetism in Hydrogenated Epitaxial Graphene*, Phys. Rev. Lett. **111**, 166101 (2013).

[6] H. González-Herrero, J. M. Gomez-Rodriguez, P. Mallet, M. Moaied, J. J. Palacios, C. Salgado, M. M. Ugeda, J.-Y. Veuillen, F. Yndurain, and I. Brihuega, *Atomic-Scale Control of Graphene Magnetism by Using Hydrogen Atoms*, Science **352**, 437 (2016).

[7] B. Huang *et al.*, *Layer-Dependent Ferromagnetism in a van der Waals Crystal down to the Monolayer Limit*, Nature (London) **546**, 270 (2017).

[8] C. Gong *et al.*, *Discovery of Intrinsic Ferromagnetism in Two-Dimensional van der Waals Crystals*, Nature (London) **546**, 265 (2017).

[9] D. J. O'Hara *et al.*, *Room Temperature Intrinsic Ferromagnetism in Epitaxial Manganese Selenide Films in the Monolayer Limit*, Nano Lett. **18**, 3125 (2018).

[10] J. Mannhart and D. G. Schlom, *Oxide Interfaces—An Opportunity for Electronics*, Science **327**, 1607 (2010).

[11] J. Z. Sun, D. W. Abraham, R. A. Rao, and C. B. Eom, *Thickness-Dependent Magnetotransport in Ultrathin Manganite Films*, Appl. Phys. Lett. **74**, 3017 (1999).

[12] M. Huijben, L. W. Martin, Y. H. Chu, M. B. Holcomb, P. Yu, G. Rijnders, D. H. A. Blank, and R. Ramesh, *Critical Thickness and Orbital Ordering in Ultrathin* $La_{0.7}Sr_{0.3}MnO_3$ *Films*, Phys. Rev. B **78**, 094413 (2008).

[13] H. Boschker, J. Verbeeck, R. Egoavil, S. Bals, G. van Tendeloo, M. Huijben, E. P. Houwman, G. Koster, D. H. A. Blank, and G. Rijnders, *Preventing the Reconstruction of the Polar Discontinuity at Oxide Heterointerfaces*, Adv. Funct. Mater. **22**, 2235 (2012).

[14] A. V. Boris *et al.*, *Dimensionality Control of Electronic Phase Transitions in Nickel-Oxide Superlattices*, Science **332**, 937 (2011).

[15] R. Scherwitzl, S. Gariglio, M. Gabay, P. Zubko, M. Gibert, and J.-M. Triscone, *Metal-Insulator Transition in Ultrathin* $LaNiO_3$ *Films*, Phys. Rev. Lett. **106**, 246403 (2011).

[16] K. Yoshimatsu, T. Okabe, H. Kumigashira, S. Okamoto, S. Aizaki, A. Fujimori, and M. Oshima, *Dimensional-Crossover-Driven Metal-Insulator Transition in* $SrVO_3$ *Ultrathin Films*, Phys. Rev. Lett. **104**, 147601 (2010).

[17] C. B. Eom, R. J. Cava, R. M. Fleming, J. M. Phillips, R. B. vanDover, J. H. Marshall, J. W. P. Hsu, J. J. Krajewski, and W. F. Peck, *Single-Crystal Epitaxial Thin Films of the isotropic Metallic Oxides* $Sr_{1-x}Ca_xRuO_3$ $(0 \leq x \leq 1)$, Science **258**, 1766 (1992).

[18] G. Koster, L. Klein, W. Siemons, G. Rijnders, J. S. Dodge, C.-B. Eom, D. H. A. Blank, and M. R. Beasley, *Structure, Physical Properties, and Applications of* $SrRuO_3$ *Thin Films*, Rev. Mod. Phys. **84**, 253 (2012).

[19] A. Kanbayasi, *Magnetic Properties of* $SrRuO_3$ *Single Crystal*, J. Phys. Soc. Jpn. **41**, 1876 (1976).

[20] P. B. Allen, H. Berger, O. Chauvet, L. Forro, T. Jarlborg, A. Junod, B. Revaz, and G. Santi, *Transport Properties, Thermodynamic Properties, and Electronic Structure of* $SrRuO_3$, Phys. Rev. B **53**, 4393 (1996).

[21] J. Choi, C.-B. Eom, G. Rijnders, H. Rogalla, and D. H. A. Blank, *Growth Mode Transition from Layer by Layer to Step Flow during the Growth of Heteroepitaxial* $SrRuO_3$ *on (001)* $SrTiO_3$, Appl. Phys. Lett. **79**, 1447 (2001).

[22] G. Rijnders, D. H. A. Blank, J. Choi, and C.-B. Eom, *Enhanced Surface Diffusion through Termination Conversion during Epitaxial* $SrRuO_3$ *Growth*, Appl. Phys. Lett. **84**, 505 (2004).

[23] H. P. Nair *et al.*, *Synthesis Science of* $SrRuO_3$ *and* $CaRuO_3$ *Epitaxial Films with High Residual Resistivity Ratios*, APL Mater. **6**, 046101 (2018).

[24] M. Izumi, K. Nakazawa, and Y. Bando, *TC Suppression of $SrRuO_3$/$SrTiO_3$ Superlattices*, J. Phys. Soc. Jpn. **67**, 651 (1998).

[25] M. Izumi, K. Nakazawa, Y. Bando, Y. Yoneda, and H. Terauchi, *Magnetic Properties of $SrRuO_3$/$SrTiO_3$ Superlattices*, Solid State Ionics **108**, 227 (1998).

[26] K. Ueda, H. Saeki, H. Tabata, and T. Kawai, *Control of the Magnetic and Electric Properties of Low-Dimensional $SrRuO_3$–$BaTiO_3$ Superlattices*, Solid State Commun. **116**, 221 (2000).

[27] D. Toyota *et al.*, *Thickness-Dependent Electronic Structure of Ultrathin $SrRuO_3$ Films Studied by In Situ Photoemission Spectroscopy*, Appl. Phys. Lett. **87**, 162508 (2005).

[28] J. Xia, W. Siemons, G. Koster, M. R. Beasley, and A. Kapitulnik, *Critical Thickness for Itinerant Ferromagnetism in Ultrathin Films of $SrRuO_3$*, Phys. Rev. B **79**, 140407 (R) (2009).

[29] Y. J. Chang, C. H. Kim, S.-H. Phark, Y. S. Kim, J. Yu, and T. W. Noh, *Fundamental Thickness Limit of Itinerant Ferromagnetic $SrRuO_3$ Thin Films*, Phys. Rev. Lett. **103**, 057201 (2009).

[30] Z. Q. Liu *et al.*, *Tailoring the Electronic Properties of $SrRuO_3$ Films in $SrRuO_3$/$LaAlO_3$ Superlattices*, Appl. Phys. Lett. **101**, 223105 (2012).

[31] S. J. Callori, J. Gabel, D. Su, J. Sinsheimer, M. V. Fernandez-Serra, and M. Dawber, *Ferroelectric $PbTiO_3$/$SrRuO_3$ Superlattices with Broken Inversion Symmetry*, Phys. Rev. Lett. **109**, 067601 (2012).

[32] F. Bern, M. Ziese, A. Setzer, E. Pippel, D. Hesse, and I. Vrejoiu, *Structural Magnetic and Electrical Properties of $SrRuO_3$ Films and $SrRuO_3$/$SrTiO_3$ Superlattices*, J. Phys. Condens. Matter **25**, 496003 (2013).

[33] P. Mahadevan, F. Aryasetiawan, A. Janotti, and T. Sasaki, *Evolution of the Electronic Structure of a Ferromagnetic Metal: Case of $SrRuO_3$*, Phys. Rev. B **80**, 035106 (2009).

[34] M. Gu, Q. Xie, X. Shen, R. Xie, J. Wang, G. Tang, D. Wu, G. P. Zhang, and X. S. Wu, *Magnetic Ordering and Structural Transitions in a Strained Ultrathin $SrRuO_3$/$SrTiO_3$ Superlattice*, Phys. Rev. Lett. **109**, 157003 (2012).

[35] J. M. Rondinelli, N. M. Caffrey, S. Sanvito, and N. A. Spaldin, *Electronic Properties of Bulk and Thin Film $SrRuO_3$: Search for the Metal-Insulator Transition*, Phys. Rev. B **78**, 155107 (2008).

[36] M. Verissimo-Alves, P. García-Fernández, D. I. Bilc, P. Ghosez, and J. Junquera, *Highly Confined Spin-Polarized Two-Dimensional Electron Gas in $SrTiO_3$/$SrRuO_3$ Superlattices*, Phys. Rev. Lett. **108**, 107003 (2012).

[37] P. García-Fernández, M. Verissimo-Alves, D. I. Bilc, P. Ghosez, and J. Junquera, *First-Principles Modeling of the Thermoelectric Properties of $SrTiO_3$/$SrRuO_3$ Superlattices*, Phys. Rev. B **86**, 085305 (2012).

[38] S. Thomas *et al.*, *Localized Control of Curie Temperature in Perovskite Oxide Film by Capping-Layer-Induced Octahedral Distortion*, Phys. Rev. Lett. **119**, 177203 (2017).

[39] W. Siemons, G. Koster, A. Vailionis, H. Yamamoto, D. H. A. Blank, and M. R. Beasley, *Dependence of the Electronic Structure of $SrRuO_3$ and Its Degree of Correlation on Cation Off-Stoichiometry*, Phys. Rev. B **76**, 075126 (2007).

[40] H. P. Nair *et al.*, *Demystifying the Growth of Superconducting Sr_2RuO_4 Thin Films*, APL Mater. **6**, 101108 (2018).

[41] D. E. Shai, C. Adamo, D. W. Shen, C. M. Brooks, J. W. Harter, E. J. Monkman, B. Burganov, D. G. Schlom, and K. M. Shen, *Quasiparticle Mass Enhancement and Temperature Dependence of the Electronic Structure of Ferromagnetic $SrRuO_3$ Thin Films*, Phys. Rev. Lett. **110**, 087004 (2013).

[42] See Supplemental Material at http://link.aps.org/supplemental/10.1103/PhysRevX.9.011027 for additional data and analysis of STEM, XRD, and torque measurements.

[43] L. Klein, Y. Kats, A. F. Marshall, J. W. Reiner, T. H. Geballe, M. R. Beasley, and A. Kapitulnik, *Domain Wall Resistivity in $SrRuO_3$*, Phys. Rev. Lett. **84**, 6090 (2000).

[44] J. Wu, J. W. Lynn, C. J. Glinka, J. Burley, H. Zheng, J. F. Mitchell, and C. Leighton, *Intergranular Giant Magnetoresistance in a Spontaneously Phase Separated Perovskite Oxide*, Phys. Rev. Lett. **94**, 037201 (2005).

[45] Y. Matsumoto *et al.*, *Room-Temperature Ferromagnetism in Transparent Transition Metal-Doped Titanium Dioxide*, Science **291**, 854 (2001).

[46] X. Renshaw Wang *et al.*, *Imaging and Control of Ferromagnetism in $LaMnO_3$/$SrTiO_3$ Heterostructures*, Science **349**, 716 (2015).

[47] L. Si, Z. Zhong, J. M. Tomczak, and K. Held, *Route to Room-Temperature Ferromagnetic Ultrathin $SrRuO_3$ Films*, Phys. Rev. B **92**, 041108(R) (2015).

[48] J. Chaloupka and G. Khaliullin, *Doping-Induced Ferromagnetism and Possible Triplet Pairing in d^4 Mott Insulators*, Phys. Rev. Lett. **116**, 017203 (2016).

[49] M. Weisheit, S. Fähler, A. Marty, Y. Souche, C. Poinsignon, and D. Givord, *Electric Field-Induced Modification of Magnetism in Thin-Film Ferromagnets*, Science **315**, 349 (2007).

[50] W. P. Zhou, Q. Li, Y. Q. Xiong, Q. M. Zhang, D. H. Wang, Q. Q. Cao, L. Y. Lv, and Y. W. Du, *Electric Field Manipulation of Magnetic and Transport Properties in $SrRuO_3$/$Pb(Mg_{1/3}Nb_{2/3})O_3 - PbTiO_{35}$ Heterostructure*, Sci. Rep. **4**, 6991 (2015).

[51] H. T. Yi, B. Gao, W. Xie, S.-W. Cheong, and V. Podzorov, *Tuning the Metal-Insulator Crossover and Magnetism in $SrRuO_3$ by Ionic Gating*, Sci. Rep. **4**, 6604 (2014).

[52] M. Jager, A. Teker, J. Mannhart, and W. Braun, *Independence of Surface Morphology and Reconstruction during the Thermal Preparation of Perovskite Oxide Surfaces*, Appl. Phys. Lett. **112**, 111601 (2018).

[53] C. D. Theis and D. G. Schlom, *Cheap and Stable Titanium Source for Use in Oxide Molecular Beam Epitaxy Systems*, J. Vac. Sci. Technol. A **14**, 2677 (1996).

[54] J. H. Haeni, C. D. Theis, and D. G. Schlom, *RHEED Intensity Oscillations for the Stoichiometric Growth of $SrTiO_3$ Thin Films by Reactive Molecular Beam Epitaxy*, J. Electroceram. **4**, 385 (2000).

[55] P. M. Voyles, J. L. Grazul, and D. A. Muller, *Imaging Individual Atoms inside Crystals with ADF-STEM*, Ultramicroscopy **96**, 251 (2003).

Ferromagnetism and conductivity in atomically thin $SrRuO_3$ – supplementary information

H. Boschker, T. Harada, T. Asaba, R. Ashoori, A.V. Boris, H. Hilgenkamp, C.R. Hughes, M.E. Holtz, L. Li, D.A. Muller, H. Nair, P. Reith, X. Renshaw Wang, D.G. Schlom, A. Soukiassian, J. Mannhart

STEM imaging and spectroscopic imaging

Scanning transmission electron microscopy and electron energy-loss spectroscopy data were recorded from mechanically polished cross-sectional specimens in the 100 keV NION UltraSTEM. Large, simultaneous spectroscopic maps of the Ru-$M_{4,5}$ edge and the Ti-$L_{2,3}$ edge were acquired with an energy dispersion of 0.25 eV/channel with a Gatan Quefina dual-EELS Spectrometer, as shown in the main text in Fig. 2. For these large spectroscopic images, we integrated components of the spectra over energies corresponding to ruthenium and titanium after a linear combination of power laws background subtraction. Because of the close proximity of the Sr-$M_{2,3}$ and Ru-$M_{4,5}$ edges, and the Ru-$M_{2,3}$ and Ti-$L_{2,3}$ edges, we used small integration windows and PCA filtering to remove noise, keeping the six components of the spectra which captured all of the spatially varying components (as discussed more for Fig. S2).

To ensure there are no artifacts with the overlapping edges or PCA filtering in determining the ruthenium distribution, we used dual EELS to acquire two energy ranges simultaneously to map the Ru-$L_{2,3}$ edge and the Ti-$L_{2,3}$ edge, shown in Fig. S1.

The high energy of the Ru-$L_{2,3}$ edge is distinct from other edges (Sr, Ti, O), making it possible to unambiguously map the ruthenium, as shown in Fig. S1. In Fig. S1(a) we show the large area image of the region chosen for this analysis, similar to regions shown in the main text. We performed EELS on a small region shown in (b), with a color map for the spectra shown in (c) with green representing titanium and purple representing ruthenium. (d) and (e) show the titanium and ruthenium signals respectively. The titanium map shows no structure in the ruthenium layer, and the ruthenium map shows the ruthenium forming a single layer. From inspection of the Ru-$L_{2,3}$ edge in Fig. S1f, we see that there is a strong peak on the ruthenium row. There also seems to be some ruthenium present on the row below (row 2), although if we inspect the spatial distribution of the edge (e.g., Fig. S2e) it appears featureless, indicating it may be due to probe tails and beam spreading. The map of the Ru-$L_{2,3}$ edge demonstrates that the ruthenium is confined to the single ruthenium layers, with minimal intensity and no structure outside these layers. This is also clear from inspecting a line profile of the ruthenium signal, Fig. S1(g), where the ruthenium is well localized to the atomic column of ruthenium. From these maps we find little intermixing between the two layers.

While unambiguous, doing mapping of the Ru-$L_{2,3}$ edge on a large field of view is prohibited by the high energy and low scattering cross section of the edge. Mapping this edge with high signal-to-noise requires long integration times and high beam doses which may damage the specimen for larger field of view images. The lower energy ruthenium edge (Ru-$M_{4,5}$) has a larger cross section and thus requires less dose to acquire high signal-to-noise data. However, the lower energy edge overlaps with Sr-$M_{2,3}$ and C-K edges (see Fig. S2f), so care must be taken to separate the

signals. Here we show our results from the low-energy edges qualitatively reproduce the results we have from the high-energy edge, as shown in Fig. S1. This implies there are no misleading artifacts in our large field of view spectroscopic maps, such as shown in the main text in Fig. 2 and in Fig. S2.

Another dataset from the spectroscopic imaging of sample A is shown in Fig. S2. Figure S2a corresponds to the simultaneous ADF image. For these spectroscopic images, we integrated components of the spectra over energies corresponding to ruthenium and titanium after a linear combination of power laws background subtraction. Because of overlapping Sr-$M_{2,3}$ and Ru-$M_{4,5}$ edges, and overlapping Ru-$M_{2,3}$ and Ti-$L_{2,3}$ (see Figs. S2e,f), the integration of the edges themselves resulted in mixed Sr-Ru or Ru-Ti signals. For ruthenium mapping, we used the post-edge features that easily distinguished ruthenium with appropriate background subtraction. The onset of the titanium edge should not be mixed with ruthenium signal, so we used a very small integration window at the onset of the edge to obtain titanium. Because of the small integration windows necessary, we used PCA filtering to remove noise, keeping six components of the spectra. Five of the six components had noticeable spatially varying features, and we kept the sixth component to ensure we did not throw away additional information. Figure S2b shows the ruthenium signal obtained by this method. Like in Fig. S1, which used the Ru-$L_{2,3}$ edge instead of the Ru-$M_{2,3}$ edge, the ruthenium signal is confined to single atomic layers of ruthenium. Figure S2c corresponds to the titanium signal, which is similarly well ordered. The color overlay shown in the main text is reproduced in Fig. S2d. The signal to noise ratio in the spectroscopic maps is 15 for titanium and 13 for ruthenium, and we clearly resolve both signals with atomic precision. Representative spectra that are averaged over a

titanium column and a ruthenium column are shown in Fig. S2f, showing the overlapping edges. Reference spectra for the edges from the Gatan EELS atlas[S1] are shown in Fig. S2g for reference. We could not determine the valence state of Ru from the fine structure of the spectra, because the Ru-$M_{4,5}$ edge overlaps with Ti and C edges and the Ru-$L_{2,3}$ edge is too high in energy. The latter does not enable us to obtain the high-signal-to-noise-ratio spectrum required for valence determination without damaging the sample. In contrast, we determined the valence state of Ti to be 4+ without any position dependence.

X-ray diffraction

Figure S3 shows a close-up of the 00(0+δ) and 00(0+2δ) superlattice reflections for both samples A and B. Next to the 00(0+δ) superlattice reflection, sample A shows some Kiessig fringes. The fringes correspond to the expected thickness of 20 $(SrRuO_3)_1$–$(SrTiO_3)_5$ repeat units. We did not observe the fringes in sample B. Also in sample A, the fringe visibility is much smaller than that expected for a perfect heterostructure. We have performed simulations with the Panalytical reflectivity software. The expected reflectivity curve for a perfect 20 times superlattice is shown as the top line in the set simulations 1. Adding interface roughness to the model does not affect the fringe visibility much. Even at a roughness of 0.4 nm per interface (much more than that deducible from the STEM data), the fringes should be clearly resolved, simulations 1 bottom line. Therefore, interface roughness cannot explain the lack of fringe visibility. The main effect of the roughness is to reduce the overall intensity at higher momentum transfer. We observe an intensity ratio of about 10 between the 00(0+δ) and 00(0+2δ) superlattice reflections. This is consistent with an interface roughness smaller than 0.2 nm.

As discussed in the main text, the superlattice reflections deviate from the expected peak positions, indicating the average thickness of the repeat unit is somewhat less than 6 unit cells. We have therefore performed simulations of a heterostructure with an 80% sample volume of $(SrRuO_3)_1$–$(SrTiO_3)_5$ and a 20% sample volume of $(SrRuO_3)_1$–$(SrTiO_3)_4$. The precise stacking of the model is as follows: 4 times $(SrRuO_3)_1$–$(SrTiO_3)_5$, 1 time $(SrRuO_3)_1$–$(SrTiO_3)_4$, 3 times $(SrRuO_3)_1$–$(SrTiO_3)_5$, 1 time $(SrRuO_3)_1$–$(SrTiO_3)_4$, 5 times $(SrRuO_3)_1$–$(SrTiO_3)_5$, 1 time $(SrRuO_3)_1$–$(SrTiO_3)_4$, 4 times $(SrRuO_3)_1$–$(SrTiO_3)_5$, and 1 time $(SrRuO_3)_1$–$(SrTiO_3)_4$. The simulation results are shown in Fig. S3, set simulations 2, as a function of interface roughness. Qualitatively the simulations capture the trends in the measurements well. The shifts in peak position are accounted for and a number of the finite thickness fringes are averaged out. The presented model is of course only a very well ordered approximation of a sample with an average $SrTiO_3$ thickness of 4.8 unit cells. Therefore we expect that these thickness variations reduce most of the fringe visibility in the samples. Due to the large amount of possible structure variations and fit parameters, we do not try to fit any curve to the experimental data.

Additional torque data

Additional torque magnetometry data is shown in Fig. S4. Figures S4a and S4b show the magnetic field dependence of the torque and derived magnetization of sample A for a larger temperature range than that depicted in Fig. 13. The magnetic hysteresis disappears at temperature above approximately 30 K, but magnetic signal remains present up to much higher temperatures. Figures S4c-h show torque data obtained from different pieces of sample B. Pieces B1 and B2 show no hysteresis but a

magnetic signal that disappears at temperatures higher than 25 K. Piece B3 shows hysteresis and measurements with the field applied close to the in-plane direction also show magnetic signal persisting up to approximately 200 K. Taken together, all pieces are ferromagnetic but they have different switching behavior. As discussed in the manuscript, the magnetic anisotropy favours a domain structure with both in-plane and out-of-plane components. The energy barriers for the switching of these components clearly differs from piece to piece. The temperature dependence of the data that shows a hysteretic part at low temperatures and magnetic signal persisting up to high temperature is in good agreement with the MR measurements.

References

S1. C.C. Ahn, and O.L. Krivanek, *EELS Atlas: A Reference Guide of Electron Energy Loss Spectra Covering All Stable Elements*. Gatan, 1983.

Figure captions

Figure S1: Spectroscopic imaging of Sample A, including the Ru-$L_{2,3}$ edge which does not overlap with any other edge in the material. (a) survey image before EELS acquisition. (b) simultaneous ADF during EELS acquisition and (c) titanium (green) and ruthenium (purple) overlays with colorbar, corresponding to the titanium map from the Ti-$L_{2,3}$ edge in (d) and the ruthenium map from the Ru-$L_{2,3}$ edge in (e), both generated by integrating the background subtracted edge. The background subtracted spectra of the Ru-$L_{2,3}$ edge are shown in (f) for each layer of the material, showing a strong Ru peak on the Ru layer. While there is a small Ru peak on layer 2, the Ru image (e) shows no structure so we believe this may be attributable to probe tails or

beam spreading from the Ru layer. (g) shows the line profile of the ruthenium over the layers.

Figure S2: Spectroscopic imaging of Sample A (same data set as in Fig. 1 in the main text). (a) simultaneous HAADF image acquired during the spectroscopic acquisition. (b) The ruthenium map from the $M_{4,5}$ edge and (c) the titanium map from the $L_{2,3}$ extracted using a linear combination of power law background fit on PCA filtered data, retaining 6 components. The ruthenium was extracted from the tail of the $M_{4,5}$ edge, and the titanium was extracted from the first 1.5 eV of the Ti edge. (d) A color overlay of the titanium and ruthenium signals, with titanium in green and ruthenium in purple, as shown with the colorbar and colormap used in (e). (f) background subtracted, PCA filtered EELS spectra on a ruthenium column and on a titanium column. (g) reference spectra taken from the Gatan EELS atlas (ref S1).

Figure S3: XRD reflectivity of samples A and B together with simulations. The curves have been offset for clarity. The set of simulations 1 were performed by assuming a perfect $(SrRuO_3)_1$–$(SrTiO_3)_5$ superlattice with 20 repeats. The different curves in the set correspond to interface roughnesses of 0 (top line), 0.2 (middle line) and 0.4 (bottm line) nm, respectively. The set of simulations 2 were performed by assuming an 80% sample volume of $(SrRuO_3)_1$–$(SrTiO_3)_5$ and a 20% sample volume of $(SrRuO_3)_1$–$(SrTiO_3)_4$. The interface roughness values are identical to set 1.

Figure S4: Torque magnetometry performed on pieces of samples A and B at different temperatures. **(a,b)** Torque and projected magnetization τ/H as a function of applied field for piece A1. Here H is applied 20 degrees away from the in-plane direction. **(c,d)** piece B1. Here H is applied 20 degrees away from the out-of-plane direction. **(e,f)** piece B2. Here H is applied 20 degrees away from the out-of-plane direction. **(g,h)** piece B3. Here H is applied 20 degrees away from the out-of-plane direction.

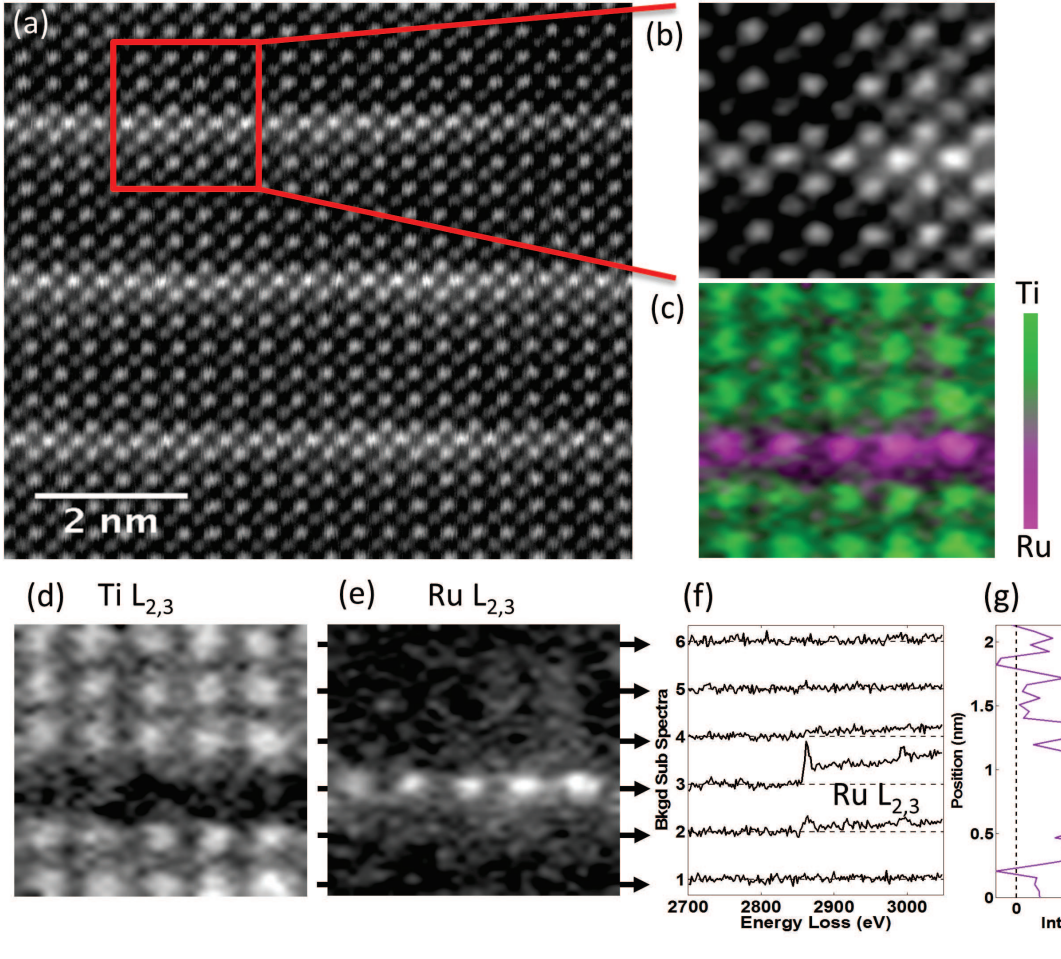
(a)
2 nm
(b)
(c)
Ti
Ru
(d) Ti L2,3
(e) Ru L2,3
(f)
Bkgd Sub Spectra
Ru L2,3
Energy Loss (eV)
(g)
Ru
Position (nm)
Intensity (arb. units)

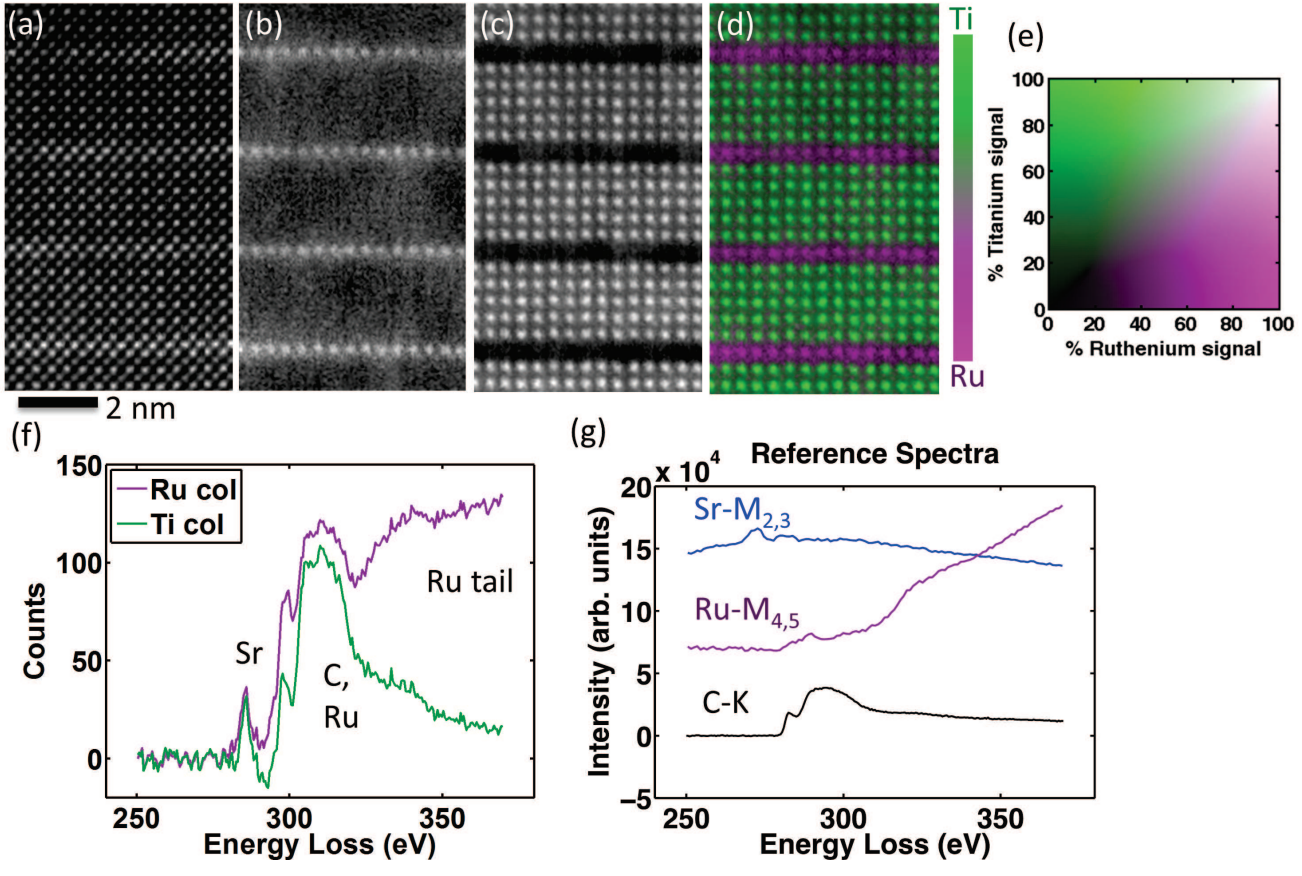
(a)
(b)
(c)
(d)
Ti
Ru
(e)
100
80
60
40
20
0
% Titanium signal
0
20
40
60
80
100
% Ruthenium signal
2 nm
(f)
150
100
50
0
Counts
Ru col
Ti col
Ru tail
Sr
C,
Ru
250
300
350
Energy Loss (eV)
(g)
Reference Spectra
x 10^4
20
15
10
5
0
−5
Intensity (arb. units)
Sr-M2,3
Ru-M4,5
C-K
250
300
350
Energy Loss (eV)

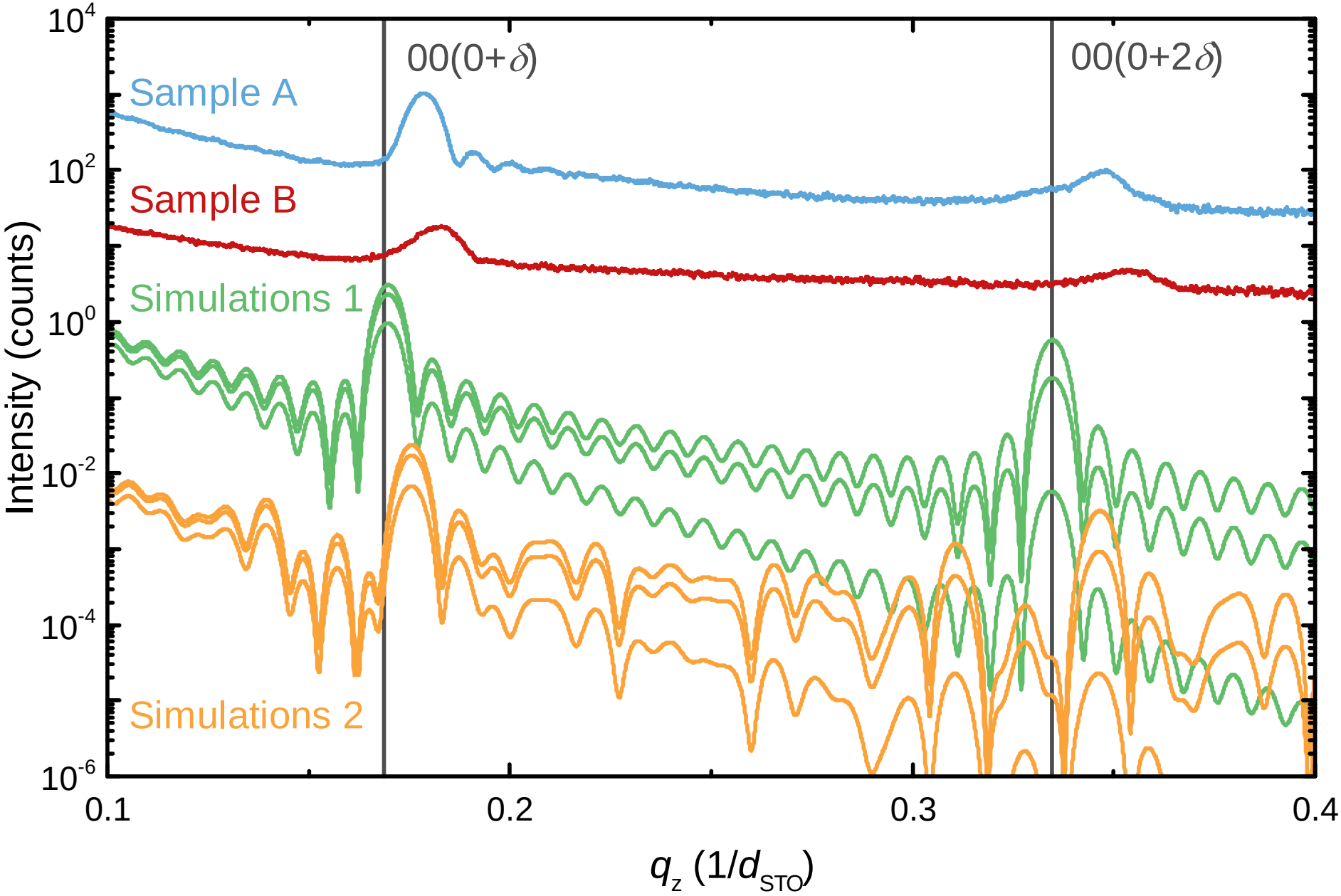
Sample A
Sample B
Simulations 1
Simulations 2
00(0+δ)
00(0+2δ)
Intensity (counts)
10^{4}
10^{2}
10^{0}
10^{-2}
10^{-4}
10^{-6}
0.1
0.2
0.3
0.4
q_z (1/d_{STO})

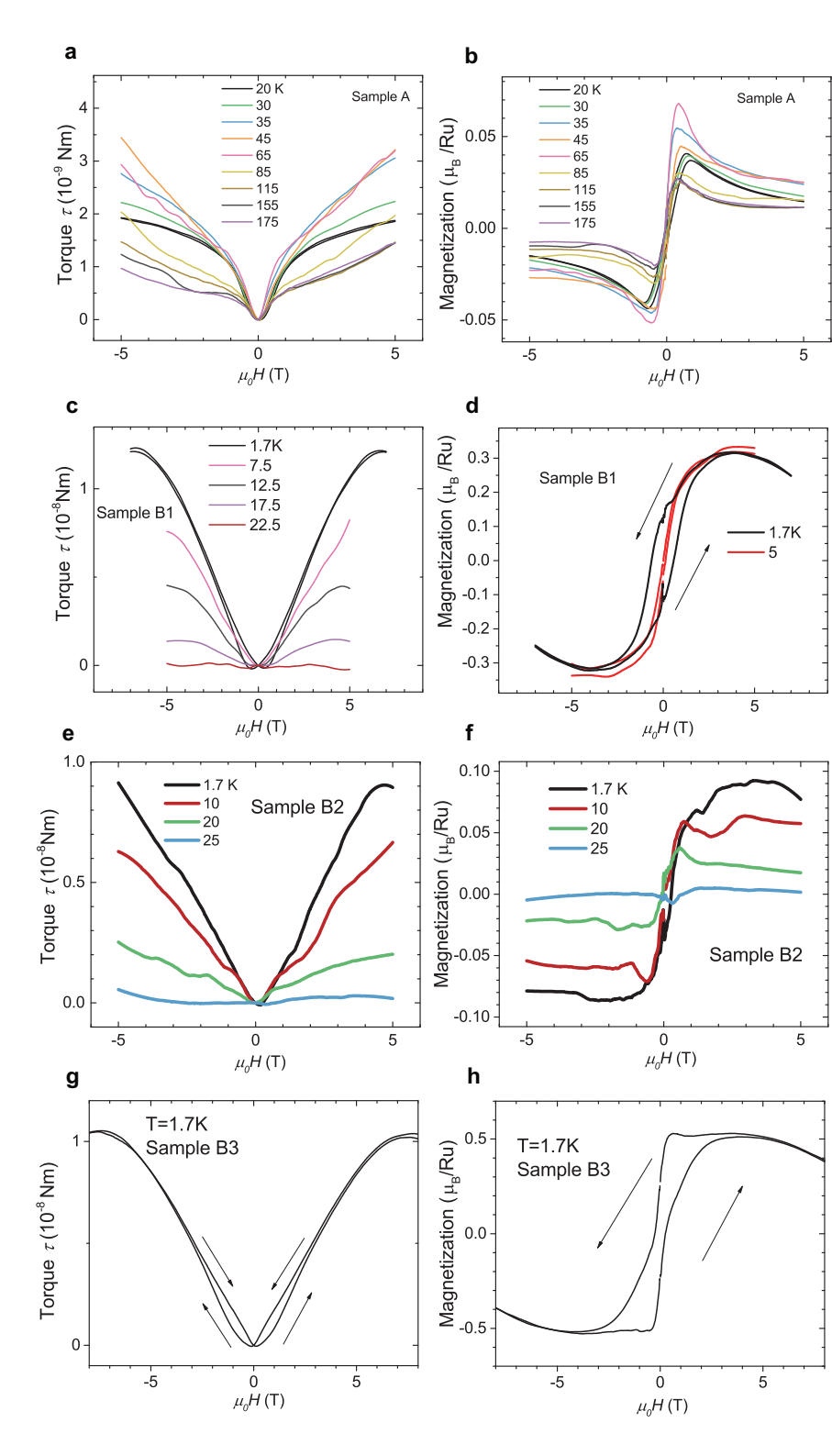
a
Torque τ (10^-9 Nm)
20 K
30
35
45
65
85
115
155
175
Sample A
μ0H (T)
b
Magnetization (μB /Ru)
20 K
30
35
45
65
85
115
155
175
Sample A
μ0H (T)
c
Torque τ (10^-8Nm)
Sample B1
1.7K
7.5
12.5
17.5
22.5
μ0H (T)
d
Magnetization (μB /Ru)
Sample B1
1.7K
5
μ0H (T)
e
Torque τ (10^-8Nm)
1.7 K
10
20
25
Sample B2
μ0H (T)
f
Magnetization (μB/Ru)
1.7 K
10
20
25
Sample B2
μ0H (T)
g
Torque τ (10^-8 Nm)
T=1.7K
Sample B3
μ0H (T)
h
Magnetization (μB/Ru)
T=1.7K
Sample B3
μ0H (T)